

# The masses of the cataclysmic variables AC Cancri and V363 Aurigae

T. D. Thoroughgood,<sup>1\*</sup> V. S. Dhillon,<sup>1</sup> C. A. Watson,<sup>1</sup> D. A. H. Buckley,<sup>2</sup>  
D. Steeghs,<sup>3</sup> M. J. Stevenson,<sup>1</sup>

<sup>1</sup>*Department of Physics and Astronomy, University of Sheffield, Sheffield, S3 7RH, UK*

<sup>2</sup>*South African Astronomical Observatory, PO Box 9, Observatory 7935, Cape Town, South Africa*

<sup>3</sup>*Harvard-Smithsonian Center for Astrophysics, 60 Garden Street, MS-67, Cambridge, MA 02138, USA*

Accepted for publication in the Monthly Notices of the Royal Astronomical Society

2 February 2008

## ABSTRACT

We present time-resolved spectroscopy and photometry of the double-lined eclipsing cataclysmic variables AC Cnc and V363 Aur (= Lanning 10). There is evidence of irradiation on the inner hemisphere of the secondary star in both systems, which we correct for using a model that reproduces the observations remarkably well. We find the radial velocity of the secondary star in AC Cnc to be  $K_R = 176 \pm 3 \text{ km s}^{-1}$  and its rotational velocity to be  $v \sin i = 135 \pm 3 \text{ km s}^{-1}$ . From these parameters we obtain masses of  $M_1 = 0.76 \pm 0.03 M_\odot$  for the white dwarf primary and  $M_2 = 0.77 \pm 0.05 M_\odot$  for the K2  $\pm$  1V secondary star, giving a mass ratio of  $q = 1.02 \pm 0.04$ . We measure the radial and rotational velocities of the G7  $\pm$  2V secondary star in V363 Aur to be  $K_R = 168 \pm 5 \text{ km s}^{-1}$  and  $v \sin i = 143 \pm 5 \text{ km s}^{-1}$  respectively. The component masses of V363 Aur are  $M_1 = 0.90 \pm 0.06 M_\odot$  and  $M_2 = 1.06 \pm 0.11 M_\odot$ , giving a mass ratio of  $q = 1.17 \pm 0.07$ . The mass ratios for AC Cnc and V363 Aur fall within the theoretical limits for dynamically and thermally stable mass transfer. Both systems are similar to the SW Sex stars, exhibiting single-peaked emission lines with transient absorption features, high-velocity S-wave components and phase-offsets in their radial velocity curves. The Balmer lines in V363 Aur show a rapid increase in flux around phase 0 followed by a rapid decrease, which we attribute to the eclipse of an optically thick region at the centre of the disc. This model could also account for the behaviour of other SW Sex stars where the Balmer lines show only a shallow eclipse compared to the continuum.

**Key words:** accretion, accretion discs – binaries: eclipsing – binaries: spectroscopic – stars: individual: AC Cnc – stars: individual: V363 Aur – novae, cataclysmic variables.

## 1 INTRODUCTION

Cataclysmic variables (CVs) are close binary stars consisting of a red dwarf secondary transferring material onto a white dwarf primary via an accretion disc or magnetic accretion stream. AC Cnc and V363 Aur are both examples of nova-likes (NLs), defined as CVs which have never been observed to undergo nova or dwarf-nova type outbursts. See Warner (1995a) for a comprehensive review of CVs.

A knowledge of the masses of the component stars in CVs is fundamental to our understanding of the origin, evolution and behaviour of these systems. Population synthesis models and the disrupted magnetic braking model of CV evolution can be observationally tested only if the number of reliably known CV masses increases. One of the most reliable ways to measure the masses of CVs is to use the radial velocity and the rotational broadening of the secondary star in eclipsing systems; the radial velocity of the disc emission lines may not represent the white dwarf's orbital motion. At present, reliable masses are known for only

\* E-mail: Tim.Thoroughgood@shef.ac.uk

~20 CVs, partly due to the difficulties in measurement (see Smith & Dhillon 1998 for a review).

AC Cnc was classified as an eclipsing variable star by Kurochkin & Shugarov (1980) with an orbital period of 7.2 hours. Shugarov (1981) suggested that AC Cnc is a NL based on *UBV* colours, and the CV nature of AC Cnc was confirmed spectroscopically by Okazaki, Kitamura & Yamasaki (1982) through broad H and He emission lines and the later study of Yamasaki, Okazaki & Kitamura (1983). Downes (1982) discovered secondary star features in the spectra leading to the first mass determination by Schlegel, Kaitchuck & Honeycutt (1984), who found  $M_1 = 0.82 \pm 0.13 M_\odot$  and  $M_2 = 1.02 \pm 0.14 M_\odot$  from the radial velocities of the primary and secondary components.

V363 Aur (= Lanning 10) was discovered by Lanning (1973) as a UV-bright source and later found to be a CV through broad Balmer and HeII emission by Margon & Downes (1981), and its typical CV energy distribution (Szkody & Crosa 1981). Horne, Lanning & Gomer (1982) obtained the first spectroscopic and photometric data, finding that V363 Aur is an eclipsing system with a period of 7.7 hours. Schlegel, Honeycutt & Kaitchuck (1986) calculated the component masses of V363 Aur to be  $M_1 = 0.86 \pm 0.08 M_\odot$  and  $M_2 = 0.77 \pm 0.04 M_\odot$  from the radial velocities of the HeII  $\lambda 4686\text{\AA}$  emission line and the *G*-band absorption.

The existing component masses of AC Cnc and V363 Aur use emission line radial velocity curves that exhibit phase shifts, suggesting that they could be unreliable. In addition to this, the mass ratio of AC Cnc found by Schlegel, Kaitchuck & Honeycutt (1984) of  $q = 1.24 \pm 0.08$  is the highest known of any CV and is very close to the upper limit of mass transfer stability computed by the models of Politano (1996). In this study, we present photometry and spectroscopy of AC Cnc and V363 Aur to calculate new masses using the secondary star properties alone.

## 2 OBSERVATIONS AND REDUCTION

On the nights of 2001 January 9–14 we obtained blue and red spectra of AC Cnc and V363 Aur with the 2.5-m Isaac Newton Telescope (INT) + IDS spectrometer on La Palma. The blue setup comprised of the 235-mm camera with the R1200B grating and the EEV10 CCD chip, which gave a wavelength coverage of approximately 4490–5580 $\text{\AA}$  at 0.95- $\text{\AA}$  (57 km s<sup>-1</sup>) resolution. In the red we used the 500-mm camera with the R1200Y grating and the TEK5 CCD chip resulting in a wavelength range of 6320–6720 $\text{\AA}$  at a resolution of 0.8- $\text{\AA}$  (36 km s<sup>-1</sup>). Simultaneous photometry in the Johnson–Cousins *B* and *R* bands was recorded with the 1-m Jacobus Kapteyn Telescope (JKT) using the SITe2 CCD chip. Full phase coverage was achieved for both objects – a full journal of observations is given in Table 1, including the exposure times used.

We also collected 19 spectral type templates ranging from G5V–M2V, telluric stars to remove atmospheric features and flux standards on both the INT and JKT. Seeing varied between 1.0 and 1.5 arcsec over the observing run and conditions were photometric on all nights except for January 10 when some patchy cloud was present.

The spectra and images were reduced using standard procedures (e.g. Dhillon, Jones & Marsh 1994; Thoroughgood et al. 2001). Comparison arc spectra were taken every 40–50 min to calibrate instrumental flexure. The arcs were fitted with a sixth-order polynomial in blue and a fourth-order polynomial in red with rms scatters of better than 0.01 $\text{\AA}$ . The photometry data were corrected for the effects of atmospheric extinction by subtracting the magnitude of a nearby comparison star (AC Cnc–9 and V363 Aur–3; Henden & Honeycutt 1995) and using values obtained by the CAMC telescope (Helmer & Morrison 1985). The absolute photometry is accurate to approximately  $\pm 0.5$  mJy; the relative photometry  $\pm 0.03$  mag. Slit losses were then corrected for by dividing each AC Cnc and V363 Aur spectrum by the ratio of the flux in the spectrum (summed over the whole spectral range) to the corresponding photometric flux.

## 3 RESULTS

### 3.1 Ephemeris

We derived new ephemerides for AC Cnc and V363 Aur, which are used to phase all data presented in this paper. The times of mid-eclipse were determined by fitting a parabola to the eclipse minima in the JKT data.

In the case of AC Cnc, a least-squares fit to the 29 eclipse timings listed in Table 2 (a) yields the ephemeris:

$$T_{\text{mid-eclipse}} = \text{HJD } 2451924.5368 + 0.30047747 E \pm 0.0006 \pm 0.00000004. \quad (1)$$

A least-squares fit to the 17 eclipse timings of V363 Aur listed in Table 2 (b) gives the ephemeris:

$$T_{\text{mid-eclipse}} = \text{HJD } 2444557.9514 + 0.32124187 E \pm 0.0016 \pm 0.00000008. \quad (2)$$

We see no evidence for any systematic variation in the O–C values shown in Table 2 in either AC Cnc or V363 Aur.

### 3.2 Average Spectrum

The average spectra of AC Cnc and V363 Aur are shown in Fig. 1, and in Table 3 we list fluxes, equivalent widths (EW) and velocity widths of the most prominent lines measured from the average spectra.

Both systems show broad, symmetric, single-peaked Balmer emission lines instead of the double-peaked profiles one would expect from a high inclination accretion disc, much like other nova-like systems (e.g. Warner 1995a). The HeI lines, however, are broad and double-peaked in nature. The line strength of HeII  $\lambda 4686\text{\AA}$  is much stronger in V363 Aur than AC Cnc and even more dominant than H $\beta$  emission. Another high excitation feature, the CIII/NIII  $\lambda\lambda 4640\text{--}4650\text{\AA}$  blend, is only present in V363 Aur and is very broad. The emission lines are characteristic of the SW Sex stars (e.g. Dhillon, Marsh & Jones 1997), but unlike others in this sub-class, these systems show clear secondary star features (no doubt due to their longer periods and hence earlier type secondaries). Both AC Cnc and V363 Aur show the absorption features of the neutral metals CaI, FeI and MgI, even in the average spectrum shown in Fig. 1, which

**Table 1.** Journal of observations for AC Cnc and V363 Aur. The epochs are calculated using the new ephemerides presented in this paper (equations 1 and 2).

UT Date	Object	INT setup	No. of spectra	Exposure time (s)	JKT filter	No. of images	Exposure time (s)	UT start	UT end	Epoch start	Epoch end
2001 Jan 09	V363 Aur	Red	61	300	<i>R</i>	323	30	22:35	03:55	22915.74	22916.43
2001 Jan 10	V363 Aur	Blue	39	400	<i>B</i>	272	30	20:07	04:36	22918.53	22919.63
2001 Jan 11	V363 Aur	Blue	70	400	<i>B</i>	474	30	19:33	04:06	22921.57	22922.67
2001 Jan 12	V363 Aur	Red	64	300	<i>R</i>	348	30	22:32	04:11	22925.97	22926.79
2001 Jan 12	AC Cnc	Red	33	300	<i>R</i>	179	30	04:26	07:21	-6.14	-5.74
2001 Jan 13	AC Cnc	Red	96	300	<i>R</i>	530	30	22:39	07:04	-3.31	-2.45
2001 Jan 14	AC Cnc	Blue	90	300	<i>B</i>	521	30	22:27	06:33	-0.32	0.80

has not been corrected for orbital motion. The secondary star features appear to be stronger relative to the continuum in AC Cnc than in V363 Aur. The weak feature at  $\lambda 6614\text{\AA}$  in the V363 Aur red spectrum is an interstellar absorption line.

### 3.3 Light Curves

The top panels of Fig. 2(a) and 2(b) show the *B* and *R*-band JKT light curves. The remaining panels show emission-line light curves, which were produced by subtracting a polynomial fit to the continuum and summing the residual flux. All light curves are plotted as a function of phase following our new ephemerides.

The *B* and *R*-band JKT light curves of AC Cnc show deep, symmetrical primary eclipses with out-of-eclipse magnitudes of  $14.30 \pm 0.05$  mag in *B* and  $14.00 \pm 0.05$  in *R*. The primary eclipse depth is 1.8 mag in *B* and 0.73 mag in *R*. We measured the phase half-width of eclipse at the out-of-eclipse level ( $\Delta\phi$ ) by timing the first and last contacts of the *B* and *R*-band photometry eclipses and dividing by two. Our average value of  $\Delta\phi = 0.09 \pm 0.01$  phases is smaller than, but consistent with, the value of  $0.108 \pm 0.008$  quoted in Harrop-Allin & Warner (1996). Ellipsoidal modulation of the red star is clearly present, although flaring around phases 0.3–0.4 contaminates the effect in *B*. There is also evidence for a secondary eclipse at phase 0.5. We see no evidence for a bright-spot in the light curves but flickering is present, particularly just after primary eclipse. A notable feature of the *B* and *R*-band JKT light curves is the U-shaped eclipse minima, in contrast to the V-shaped minima seen in many SW Sex systems (Knigge et al. 2000). The eclipses of the Balmer lines show the usual V-shape, but the HeII line has a U-shaped eclipse minimum and is completely eclipsed, suggesting an origin close to the white dwarf. The H $\alpha$  flux increases markedly after eclipse before slowly declining – there is also the suggestion of a sharp decrease in flux around phase 0.5. This secondary eclipse is possibly also seen in the HeI line, although the primary eclipse here is much broader and shallower. The H $\beta$  flux seems more erratic in behaviour, closely resembling the higher-excitation HeII emission line. Note that when the Balmer flux increases, the flickering in the JKT light curves is more prominent.

The V363 Aur JKT light curves in both the *B* and *R*-bands are deep and symmetrical with V-shaped eclipse minima, much like the SW Sex systems (Knigge et al. 2000). The *B*-band out-of-eclipse magnitude is  $14.50 \pm 0.10$ , and the eclipse depth is 0.88 mag; in the *R*-band, the out-of-eclipse magnitude is  $13.65 \pm 0.05$  with an eclipse

depth of 0.63 mag. Our measured phase half-width of eclipse at the out-of-eclipse level,  $\Delta\phi = 0.078 \pm 0.005$  (the average from the *B* and *R*-band photometry eclipses) is lower than the value of  $0.120 \pm 0.010$  quoted by Harrop-Allin & Warner (1996). There is evidence of either a shallow secondary eclipse or orbital modulation in the *R*-band light curve but not so in *B*. One of the most notable features of the light curves is the high level of flickering present. The red emission-line light curves of H $\alpha$  and HeI are similar in that they both show a maximum flux around phase 0.7. Perhaps the most interesting feature of the emission-line lightcurves is in the primary eclipse of the Balmer lines; the flux seems to drop entering eclipse but at phase 0 there is a sharp increase in Balmer line emission followed by a rapid decrease. This is particularly prominent in H $\beta$ , but also seems to be present in the H $\alpha$  line and possibly the HeI line. The effect is definitely not present in the high excitation HeII and CIII/NIII complex.

### 3.4 Trailed spectrum & Doppler Tomography

We subtracted polynomial fits to the continuum from the spectra and then rebinned the spectra onto a constant velocity-interval scale centred on the rest wavelength of the H $\alpha$ , H $\beta$ , HeI  $\lambda 6678\text{\AA}$  and HeII  $\lambda 4686\text{\AA}$  lines. The data were then phase-binned into 50 bins, all of which were filled except for 1 empty bin at phase 0.31–0.33 in the blue V363 Aur data set. The trailed spectra of the lines are shown in the upper panels of Fig. 3 (a) and (b). We then constructed Doppler tomograms from the trailed spectra, a technique which maps the velocity-space distribution of the emission lines (e.g. Marsh 2001). The Doppler maps are shown in Fig. 4 and trailed spectra reconstructed from the maps are presented in the lower panels of Fig. 3 (a) and (b).

The trailed spectra of AC Cnc show two clearly-defined components. The first is a high-amplitude S-wave with a semi-amplitude of  $\sim 500\text{km s}^{-1}$ , which crosses zero velocity from red to blue around phase 0.15. The emission is particularly noticable in H $\alpha$  but can be seen in the other lines. This component appears in the Doppler map superimposed upon a ring of emission characteristic of an accretion disc at  $R_D = 0.4 - 0.5L_1$ . This is what one would expect from the bright-spot, although it appears slightly downstream from where the computed gas stream joins the accretion disc, a trait also seen in other CVs (e.g. WZ Sge; Spruit & Rutten 1998). The second, lower-velocity component seen in the Balmer lines, seemingly in anti-phase with the higher-velocity component, shows up clearly in the Doppler maps as originating on the inner hemisphere of the

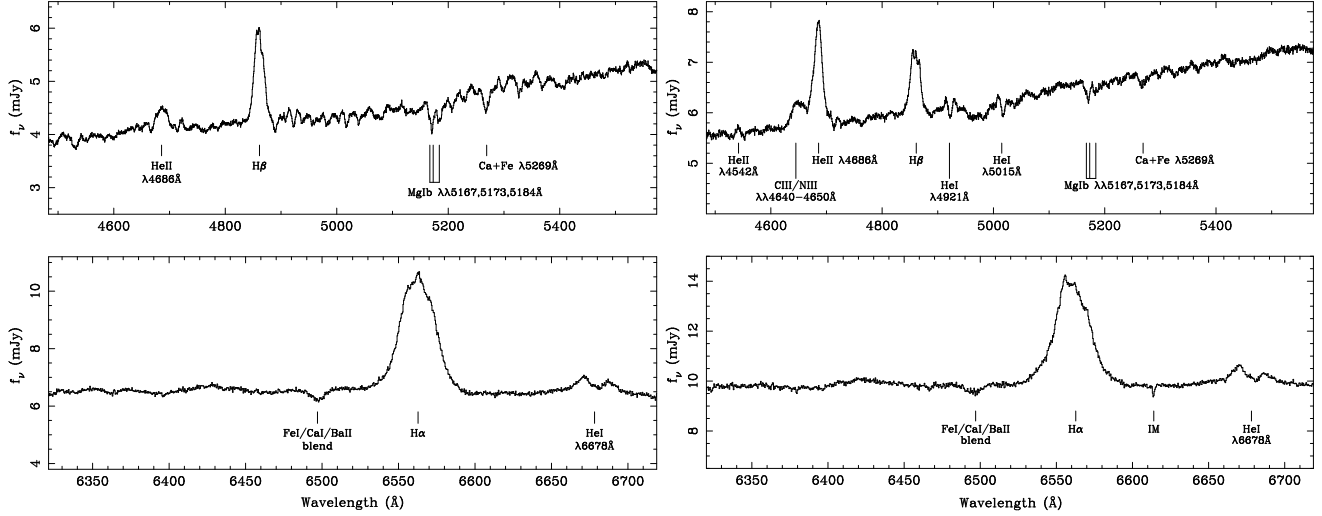


**Figure 1.** Average spectra of AC Cnc (left) and V363 Aur (right).

[h]

**Table 3.** Fluxes and widths of prominent lines in AC Cnc and V363 Aur, measured from the average spectra. In the case of V363 Aur, HeII  $\lambda 4686\text{\AA}$  and CIII/NIII  $\lambda\lambda 4640\text{--}4650\text{\AA}$  are blended, so separate values of the flux and EW are given (determined from a double-Gaussian fit) as well as the combined flux of the two.

(a) AC Cnc

Line	Flux $\times 10^{-14}$ (ergs cm $^{-2}$ s $^{-1}$ )	EW ( $\text{\AA}$ )	FWHM (km s $^{-1}$ )	FWZI (km s $^{-1}$ )
H $\alpha$	$7.57 \pm 0.01$	$16.55 \pm 0.03$	$1100 \pm 100$	$2900 \pm 500$
H $\beta$	$4.63 \pm 0.01$	$8.57 \pm 0.03$	$1250 \pm 100$	$2800 \pm 300$
HeI $\lambda 6678\text{\AA}$	$0.94 \pm 0.01$	$2.17 \pm 0.02$	$1100 \pm 100$	$1900 \pm 500$
HeII $\lambda 4686\text{\AA}$	$1.36 \pm 0.01$	$2.32 \pm 0.02$	$1600 \pm 100$	$2300 \pm 300$

(b) V363 Aur

H $\alpha$	$8.07 \pm 0.02$	$11.82 \pm 0.02$	$1150 \pm 100$	$3100 \pm 500$
H $\beta$	$3.60 \pm 0.02$	$4.88 \pm 0.02$	$1250 \pm 100$	$2900 \pm 300$
HeI $\lambda 6678\text{\AA}$	$0.86 \pm 0.01$	$1.31 \pm 0.02$	$1100 \pm 100$	$2300 \pm 500$
HeII $\lambda 4686\text{\AA}$	$4.84 \pm 0.02$	$6.19 \pm 0.03$	$1150 \pm 100$	$3400 \pm 500$
CIII/NIII $\lambda\lambda 4640\text{--}4650\text{\AA}$	$2.05 \pm 0.03$	$2.58 \pm 0.03$	$1950 \pm 100$	$4900 \pm 500$
HeII + CIII/NIII	$7.35 \pm 0.02$	$9.37 \pm 0.03$		

secondary star. There is possibly another component visible in the HeI  $\lambda 6678\text{\AA}$  line, which could be interpreted as the signature of a faint double-peaked accretion disc. All of the low-excitation lines exhibit the rotational disturbance expected from a high inclination accretion disc, but interestingly this is not seen in the HeII  $\lambda 4686\text{\AA}$  line. These emission features are very similar to those seen in the nova-like SW Sex (Dhillon, Marsh & Jones 1997).

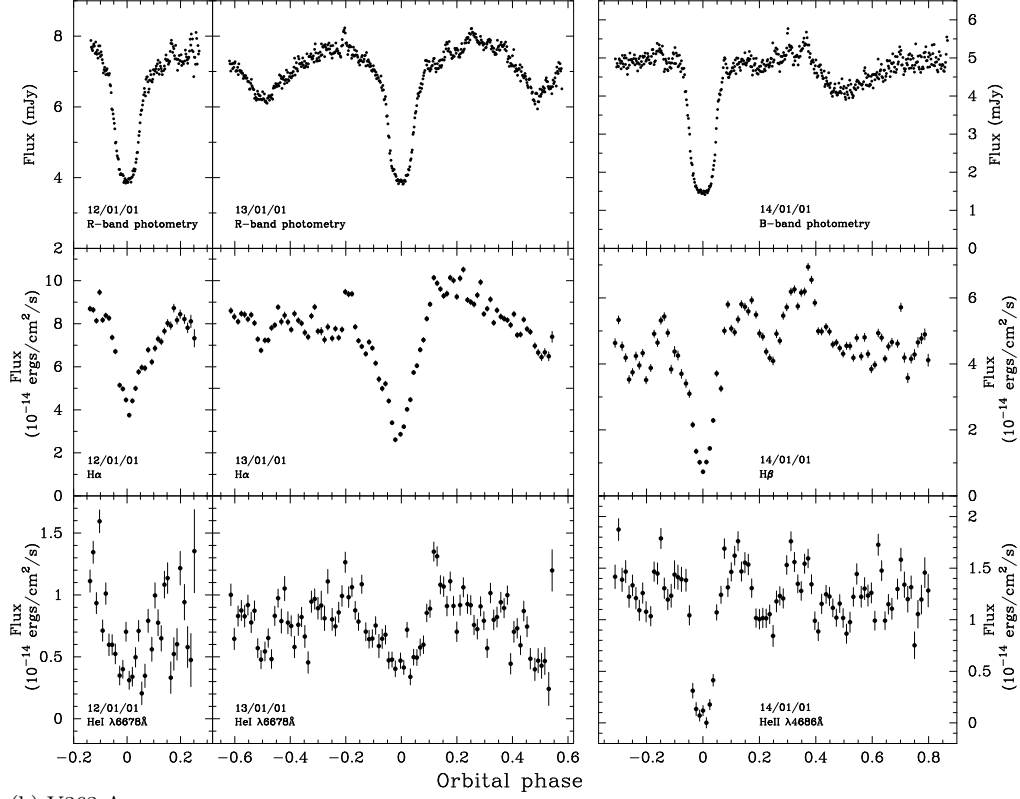
The high-amplitude S-wave and the low-amplitude emission are also seen in V363 Aur, although the anti-phase sinusoid of the secondary is less well pronounced. The high-amplitude Balmer emission in the Doppler maps appears as a bright-spot downstream from where the gas stream meets the disc, as well as from the opposite side of the disc. There is clearly Balmer emission from the inner hemisphere of the secondary which is likely to be caused by irradiation by the accretion regions or white dwarf. The HeI trailed spectrum

gives the visual impression of an absorption feature (moving at  $\sim K_W$ ) super-imposed on a high-velocity S-wave. The strange increase in Balmer line and HeI  $\lambda 6678\text{\AA}$  emission at phase zero seen in the lightcurves is clearly visible in the trailed spectra. Possible explanations for this are given in Section 4. The high-excitation HeII  $\lambda 4686\text{\AA}$  line is single-peaked throughout the orbit and the emission lies on the white dwarf centre of mass in the Doppler map.

### 3.5 Radial velocity of the white dwarf

We measured the radial velocities of the emission lines in AC Cnc and V363 Aur by applying the double-Gaussian method of Schneider & Young (1980), since this technique is sensitive mainly to the line wings and should therefore reflect the motion of the white dwarf with the highest reliability. We used Gaussians of widths 200, 300 and 400 km s $^{-1}$  and

(a) AC Cnc



(b) V363 Aur

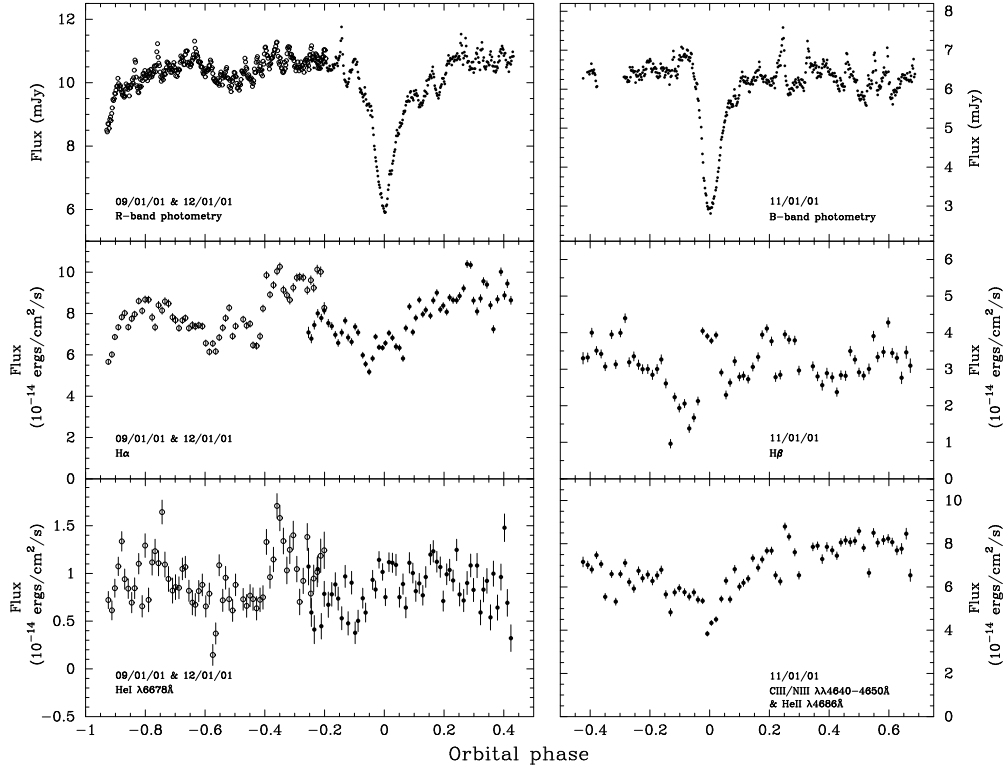
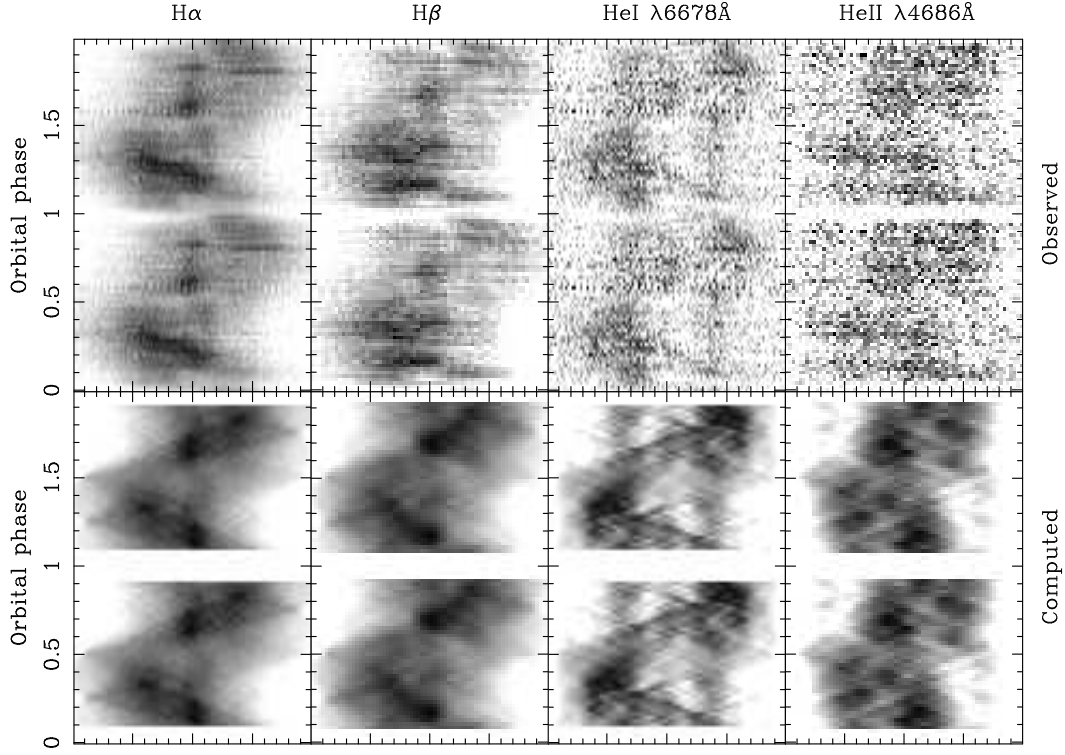


**Figure 2.** Lightcurves of (a) AC Cnc and (b) V363 Aur. Top panels: *R* and *B*-band JKT lightcurves. Middle and bottom panels: Emission-line lightcurves of  $H\alpha$ ,  $H\beta$ , CIII/NIII  $\lambda\lambda 4640\text{--}4650\text{\AA}$  + HeII  $\lambda 4686\text{\AA}$  and HeI  $\lambda 6678\text{\AA}$ . The *R*-band V363 Aur data are from 2 nights; open circles represent data from 12/01/01 and closed circles represent data from 09/01/01. Note that the two nights of data are split by orbital phase, as well as by night of observation.

(a) AC Cnc



(b) V363 Aur

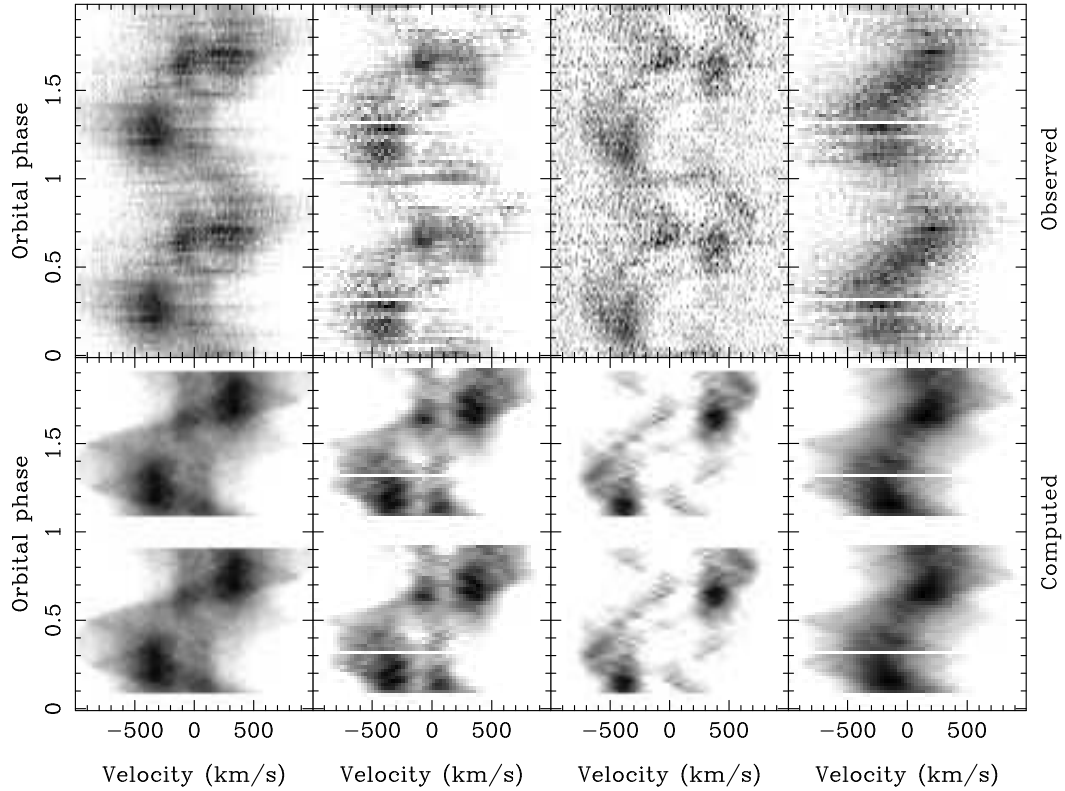


**Figure 3.** (a) Trailed spectra of AC Cnc (upper panel) & data computed from the Doppler maps (lower panel). (b) Trailed spectra of V363 Aur (upper panel) & data computed from the Doppler maps (lower panel). A comparison of the upper and lower panels gives some indication of the quality of the fit. The gaps in the computed data correspond to eclipse spectra (selected using the light curves of Fig. 2), which have been omitted from the fit as Doppler tomography cannot properly account for these phases. Note that the data have been folded to show more than one binary cycle.

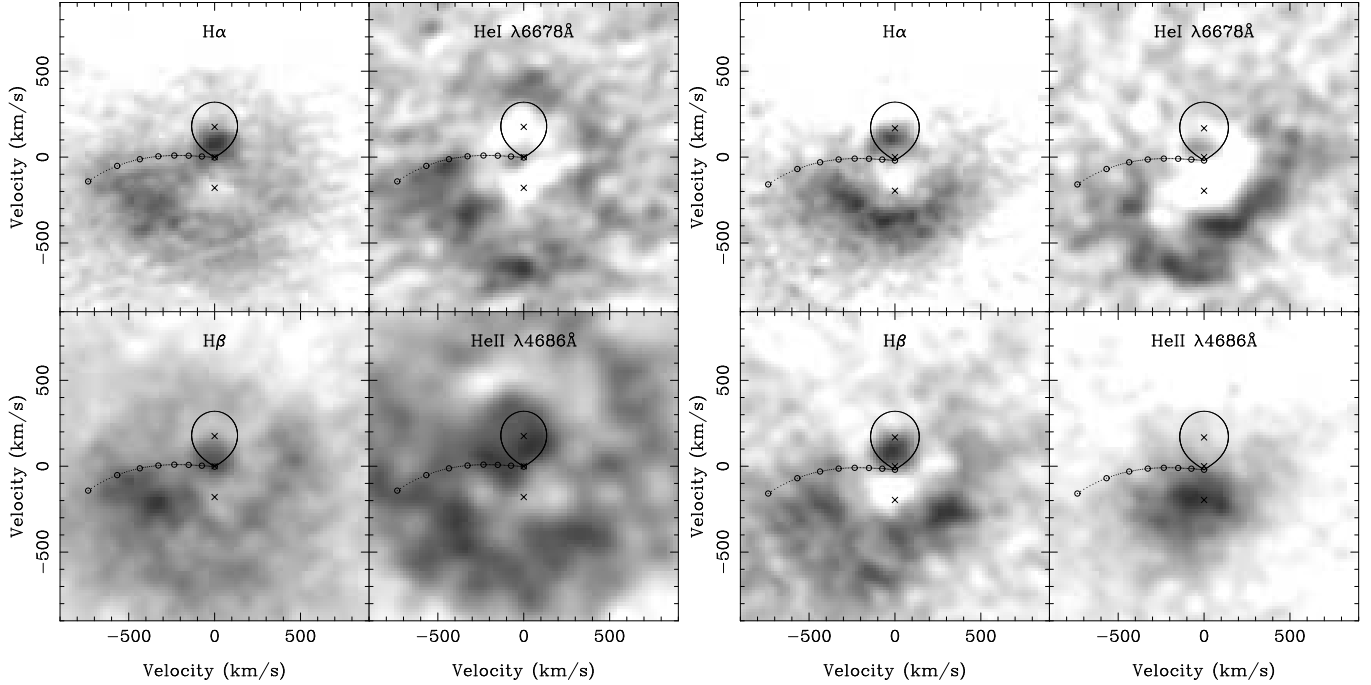


**Figure 4.** Doppler maps of emission lines in AC Cnc (left) and V363 Aur (right). The three crosses marked on each Doppler map represent the centres of mass of the secondary (upper cross), the system (middle cross) and the primary (lower cross). These crosses, the Roche lobe of the secondary star and the predicted trajectory of the gas stream have been plotted using the  $K_R$ -corrected system parameters summarised in Table 5. The series of circles along the gas stream mark the distance from the white dwarf at intervals of  $0.1L_1$ , ranging from  $1.0L_1$  at the red star to  $0.3L_1$ .

varied their separation from 200 to  $2500 \text{ km s}^{-1}$ . We then fitted

$$V = \gamma - K \sin[2\pi(\phi - \phi_0)] \quad (3)$$

to each set of measurements, where  $V$  is the radial velocity,  $K$  the semi-amplitude,  $\phi$  the orbital phase, and  $\phi_0$  is the phase at which the radial velocity curve crosses from red to blue.

Examples of the radial velocity curves for AC Cnc and V363 Aur are shown in Fig. 5. The most striking feature of all of the radial velocity curves are the phase shifts, where the spectroscopic conjunction of each line occurs after photometric eclipse. This phase shift implies an emission line source trailing the accretion disc, such as a bright spot, and is a common feature of SW Sex stars (e.g. DW UMa, Shafter, Hessman & Zhang 1988; V1315 Aql, Dhillon, Marsh & Jones 1991; SW Sex, Dhillon, Marsh & Jones 1997). There is clear evidence of rotational disturbance in the Balmer lines of AC Cnc, where the radial velocities measured just prior to eclipse are skewed to the red, and those measured after eclipse are skewed to the blue. This confirms the detection of a similar feature in the trailed spectra, and indicates that at least some of the emission must originate in the disc. We tried to measure white dwarf radial velocity ( $K_W$ ) values from the emission lines in AC Cnc and V363 Aur using a diagnostic diagram (e.g. Shafter, Szkody & Thorstensen 1986) and a light centres diagram (e.g. Marsh 1988) but with no success. This is not surprising given that the Doppler maps (Fig. 4) show that the accretion disc does not dominate the

emission in these systems. We conclude that the emission lines of AC Cnc and V363 Aur are unreliable indicators of the white dwarf radial velocity due to the phase shifts.

### 3.6 Radial velocity of the secondary star

The secondary star in both AC Cnc and V363 Aur is clearly visible in Fig. 1 through absorption lines of MgI, FeI and CaI. We compared regions of the spectra rich in absorption lines with a number of red dwarfs of spectral types G5V–M2V. A technique known as skew mapping was used to enhance the secondary features and obtain a radial velocity ( $K_R$ ) measurement (see Vande Putte et al. (2003) for a detailed critique of the method and Smith, Dhillon & Marsh (1998) for a successful application to BT Mon).

The first step was to shift the spectral type template stars to correct for their radial velocities. We then normalized each spectrum by dividing by a first-order polynomial fit, and then subtracting a higher order fit to the continuum. This ensures that line strength is preserved along the spectrum. The AC Cnc and V363 Aur spectra were normalized in the same way. The template spectra were artificially broadened to account for the orbital smearing of the CV spectra due to their exposure times ( $t_{exp}$ ) using the formula

$$V = \frac{t_{exp} 2\pi K_R}{P} \quad (4)$$

(e.g. Watson & Dhillon 2001), and then by the rotational velocity of the secondary ( $v \sin i$ ). Estimated values of  $K_R$  and  $v \sin i$  were used in the first instance, before iterating

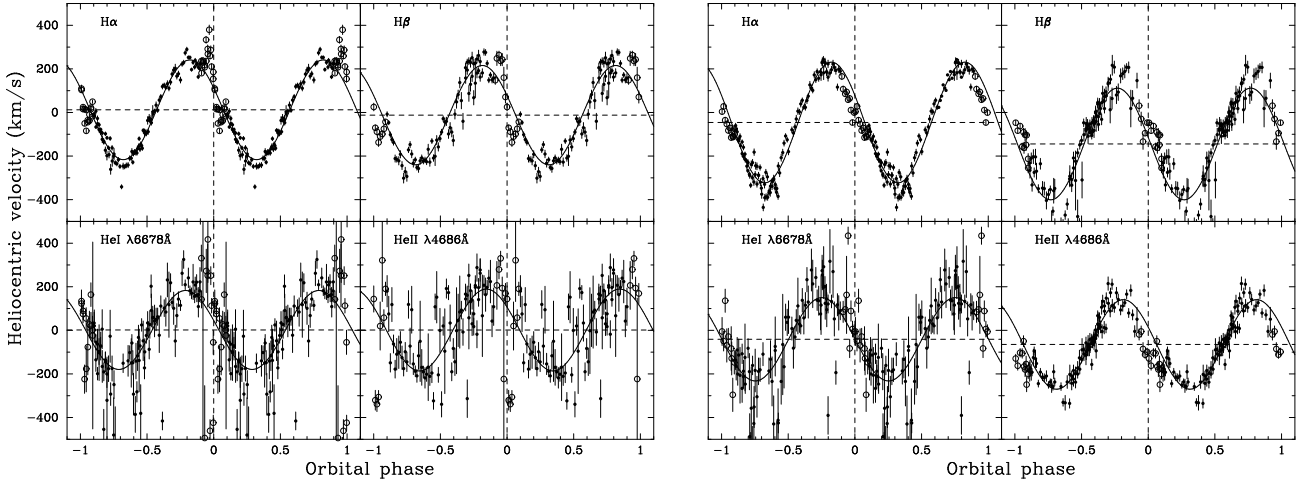


**Figure 5.** Radial velocity curves of the emission lines in AC Cnc using Gaussian widths of  $200 \text{ km s}^{-1}$  and a separation of  $1200 \text{ km s}^{-1}$  (left), and of V363 Aur using Gaussian widths of  $300 \text{ km s}^{-1}$  and a separation of  $1200 \text{ km s}^{-1}$  (right). We omitted the points around primary eclipse (open circles) during the fitting procedure as these measurements are affected by the rotational disturbance. The horizontal dashed lines represent the  $\gamma$  velocities given by the sinusoidal fits.

to find the best-fitting values given in Section 3.10. Regions of the spectrum devoid of emission lines were then cross-correlated with each of the templates yielding a time series of cross-correlation functions (CCFs) for each template star. To produce the skew maps, these CCFs were back-projected in the same way as time-resolved spectra in standard Doppler tomography (Marsh & Horne 1988). If there is a detectable secondary star, we expect a peak at  $(0, K_R)$  in the skew map. This can be repeated for each of the templates, and the final skew map is the one that gives the strongest peak.

The AC Cnc skew maps show well-defined peaks at  $K_y \approx 186 \text{ km s}^{-1}$  – the skew map for the K2V template is shown in Fig. 6 together with the trailed CCFs and the regions used for the cross-correlation can be seen in Fig. 7. A systemic velocity of  $\gamma = 40 \text{ km s}^{-1}$  was applied in order to shift the skew map peaks onto the  $K_x = 0$  axis. The  $K_R$  value varies little with  $\gamma$  in practice, as  $K_x \ll K_y$  in the back-projections (e.g. Smith, Dhillon & Marsh 1998). We adopt  $\gamma = 40 \pm 5 \text{ km s}^{-1}$  as the systemic velocity of the AC Cnc, in contrast to values of  $122 \text{ km s}^{-1}$  and  $107 \text{ km s}^{-1}$  found by Schlegel, Kaitchuck & Honeycutt (1984) using Balmer emission lines. Our adopted  $K_R$  value of  $186 \pm 3 \text{ km s}^{-1}$  is derived from the best-fitting template (K2V), with the error incorporating the spread of values obtained by using different templates (see Table 4). The uncertainty also reflects the scatter in the radial velocity fits shown in Fig. 8. Note the remarkable agreement in the  $(K_y, K_x)$  values obtained from the red and blue data sets in Table 4. The small scatter in  $K_y$  assures us that  $K_R$  is robust, and the small scatter in  $K_x$  around zero indicates that our assumed  $\gamma$  is correct.

The final V363 Aur skew maps for the G7V template (blue) and G5V template (red) and trailed CCFs are shown in Fig. 6, with the regions used for the cross-correlation marked in Fig. 7. For V363 Aur, the systemic velocity was less simple to determine, as the blue skew map suggested  $\gamma = -10 \text{ km s}^{-1}$  and the red skew map gave  $\gamma =$

$10 \text{ km s}^{-1}$ . We can find no explanation for this discrepancy, so adopt a systemic velocity of  $\gamma = 0 \pm 10 \text{ km s}^{-1}$ . Schlegel, Honeycutt & Kaitchuck (1986) find systemic velocities ranging from  $10 \pm 3 \text{ km s}^{-1}$  for the HeII  $\lambda 4686 \text{ \AA}$  line-wings to  $35 \pm 3 \text{ km s}^{-1}$  for the G-band absorption line. However, the peaks in the skew maps appear consistently at  $K_y \approx 184 \text{ km s}^{-1}$ . Our adopted value of  $K_R = 184 \pm 5 \text{ km s}^{-1}$  once again acknowledges the uncertainty in using different templates and the scatter in the radial velocity curves.

### 3.7 Rotational velocity and spectral type of the secondary star

In order to maximise the strength of the secondary features, we averaged the orbitally-corrected eclipse spectra of AC Cnc and V363 Aur. The spectral-type templates were broadened for smearing due to orbital motion as before and rotationally broadened by a range of velocities ( $50$ – $240 \text{ km s}^{-1}$ ). We then ran an optimal subtraction routine, which subtracts a constant times the normalized template spectrum from the normalized, orbitally-corrected CV spectrum, adjusting the constant to minimize the residual scatter between the spectra. The scatter is measured by carrying out the subtraction and then computing the  $\chi^2$  between the residual spectrum and a smoothed version of itself. By finding the value of rotational broadening that minimizes the  $\chi^2$ , we obtain an estimate of both  $v \sin i$  and the spectral type of the secondary star. Note that the  $v \sin i$  values of the template stars are much lower than the instrumental resolution, so do not affect our measurements of  $v \sin i$  for the secondary star.

The value of  $v \sin i$  obtained using this method varies depending on the spectral type template, the wavelength region for optimal subtraction, the amount of smoothing of the residual spectrum in the calculation of  $\chi^2$  and the value of the limb-darkening coefficient used in the broadening procedure. The values of  $v \sin i$  found from the G and K



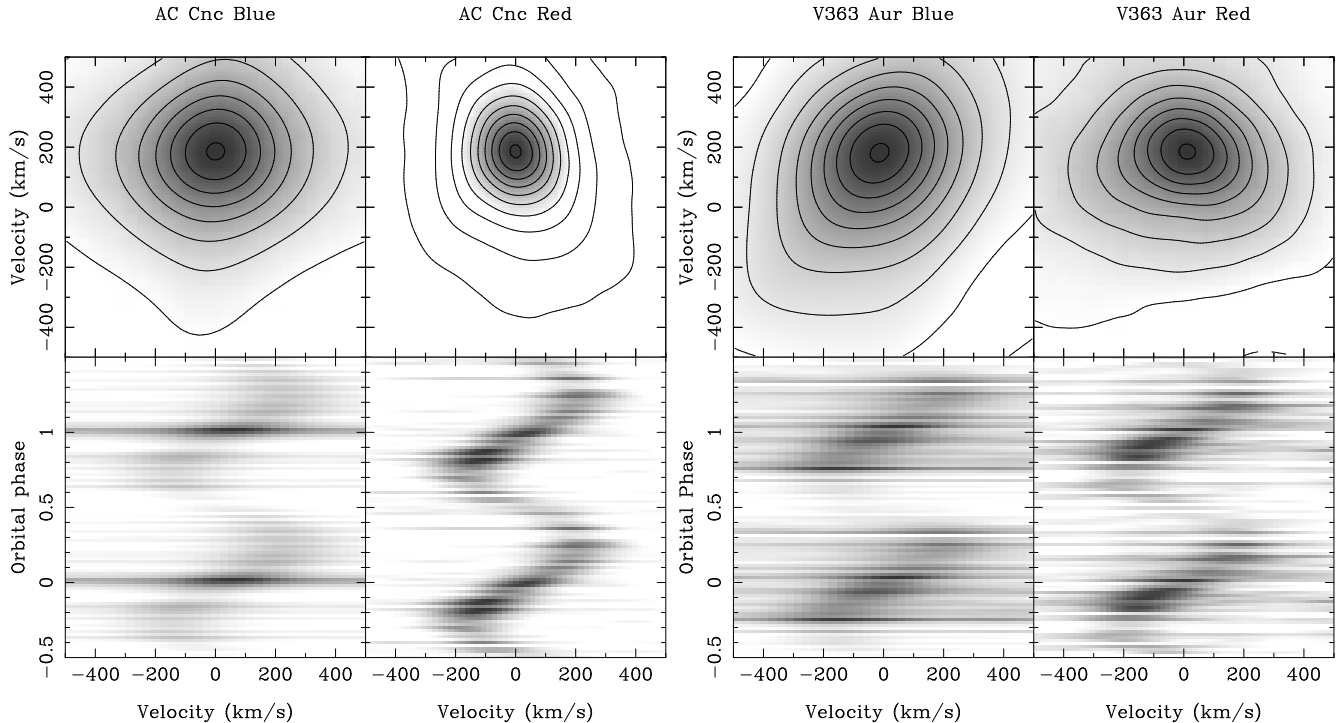


**Figure 6.** Left: Skewmaps and trailed CCFs of AC Cnc, measured using a K2V template. Right: Skewmaps and trailed CCFs of V363 Aur, measured using a G7V template in the blue and a G5V template in the red.

templates in the red and blue wavelength ranges, calculated using a limb-darkening coefficient of 0.5 and smoothed using a Gaussian of  $\text{FWHM} = 15 \text{ km s}^{-1}$ , are listed in Table 4, together with the minimum  $\chi^2$ . The optimal subtraction technique also tells us the value of the constant by which the template spectra were multiplied, which, for normalized spectra, is the fractional contribution of the secondary star to the total light in eclipse. These results are also summarised in Table 4.

For AC Cnc, the spectral types with the lowest  $\chi^2$  values are G7V and K2V in blue and G9V in red, by no means offering a definitive answer. However, the fractional contribution of the secondary star must be less than one, ruling out a G type companion. By visually inspecting each of the spectra, we settle on a spectral type for the secondary star in AC Cnc of  $\text{K2} \pm 1\text{V}$ . A plot of the AC Cnc average eclipse spectrum, a broadened template spectrum and the residual of the optimal subtraction is shown in Fig. 7. The analysis using a K2V template results in a  $v \sin i$  measurement of  $136 \text{ km s}^{-1}$  in blue and  $134 \text{ km s}^{-1}$  in red, prompting us to adopt  $v \sin i = 135 \pm 3 \text{ km s}^{-1}$ . This encompasses the  $v \sin i$  value for all the G and early-mid K templates (except for the blue G5V) within  $2\sigma$ . The error also reflects all of the other variations noted at the beginning of the previous paragraph. Schlegel, Kaitchuck & Honeycutt (1984) conclude that the secondary is a late G or early K star, not later than K3. We further limit this to an early K star, most likely K2V, agreeing with the studies of Yamasaki, Okazaki & Kitamura (1983) and Zhang (1987). The results, however, conflict with the K5 estimate of Shugarov (1981) based on *UBV* colours. We find that, in eclipse, the secondary star in AC Cnc contributes  $85 \pm 5$

per cent of the total light in the blue and  $74 \pm 19$  per cent in the red, assuming a  $\text{K2} \pm 1\text{V}$  spectral type.

For V363 Aur, the G7V template yields the lowest  $\chi^2$  value in blue, and the G5V proves the best in red. Unfortunately, we did not record spectra of the G6V and G7V templates in red, so we can only conclude from this analysis and by visual inspection that V363 Aur has a secondary of  $\text{G7} \pm 2\text{V}$ . The average  $v \sin i$  is  $147 \pm 5 \text{ km s}^{-1}$  in the blue and  $139 \pm 5 \text{ km s}^{-1}$  in the red. We therefore adopt a compromise value of  $v \sin i = 143 \pm 5 \text{ km s}^{-1}$ , encompassing all  $v \sin i$  measurements for a G or early-mid K type secondary star. Schlegel, Honeycutt & Kaitchuck (1986) conclude that the spectral type is late G, and can be no later than K3, in agreement with this study. We do, however, rule out the estimate of a G0V star by Szkody & Crosa (1981). Using our adopted spectral type of  $\text{G7} \pm 2\text{V}$ , we find that in eclipse the secondary contributes  $25 \pm 3$  per cent of the light in the blue and  $45 \pm 8$  per cent in the red.

At first glance, the fractional contributions of the secondary stars in the two systems during eclipse appear to be inconsistent. The  $\text{K2} \pm 1\text{V}$  secondary star in AC Cnc contributes a larger fraction in blue than red, whereas the (intrinsically bluer)  $\text{G7} \pm 2\text{V}$  secondary in V363 Aur contributes a smaller fraction. This can be explained by considering the different geometries of the two systems. In AC Cnc, almost all of the disc is obscured during eclipse, leaving only the redder outer disc uneclipsed. In V363 Aur, however, a large portion of the blue inner parts of the disc are still visible during eclipse (seen in Fig. 11), contributing significantly to the blue eclipse light. Outside eclipse, we measure the fractional contribution of the secondary star in AC Cnc to be  $19 \pm 2$  per cent in blue and  $40 \pm 11$  per cent in red.

[h]

**Table 2.** (a) Times of mid-eclipse for AC Cnc according to Kurochkin & Shugarov (1980; KS80), Yamasaki, Okazaki & Kitamura (1983; YOK83), Schlegel, Kaitchuck & Honeycutt (1984; SKH84), Zhang (1987; Z87) and this paper. (b) Times of mid-eclipse for V363 Aur according to Horne, Lanning & Gomer (1982; HLG82), Schlegel, Honeycutt & Kaitchuck (1986; SHK86), Rutten, van Paradijs & Tinbergen (1992; RvPT92) and this paper. The uncertainties on the mid-eclipse times measured from our data are 0.001; all other uncertainties are taken to be 0.005.

(a) AC Cnc

Cycle (E)	HJD at mid-eclipse (2,400,000+)	O-C (secs)	Reference
-59456	34059.348	-37.03	KS80
-50866	36640.446	-336.27	KS80
-50813	36656.367	-708.29	KS80
-47342	37699.327	-474.74	KS80
-33860	41750.380	886.55	KS80
-31241	42537.320	-20.02	KS80
-30136	42869.344	-331.40	KS80
-29177	43157.504	-149.38	KS80
-29074	43188.450	-424.07	KS80
-29061	43192.362	76.43	KS80
-29038	43199.275	250.81	KS80
-28848	43256.368	447.87	KS80
-28785	43275.293	8.90	KS80
-28165	43461.579	-857.79	KS80
-26867	43851.619	891.34	KS80
-26598	43932.439	162.19	KS80
-26588	43935.443	95.25	KS80
-26578	43938.448	114.72	KS80
-26525	43954.376	347.49	KS80
-23098	44984.1119	313.96	YOK83
-23094	44985.3141	339.02	YOK83
-23088	44987.1165	298.86	YOK83
-21522	45457.6637	254.17	SKH84
-19342	46112.7032	134.62	Z87
-19335	46114.8053	27.29	Z87
-19312	46121.7177	149.82	Z87
-6	51922.7339	-8.03	This Paper
-3	51923.6350	-36.75	This Paper
0	51924.5367	-13.63	This Paper

(b) V363 Aur

0	44557.9495	-168.03	HLG82
3	44558.9128	-204.81	HLG82
6	44559.8772	-146.54	HLG82
105	44591.6813	-46.80	HLG82
106	44592.0023	-67.70	HLG82
4694	46065.8614	51.42	SHK86
4700	46067.7877	-48.05	SHK86
4703	46068.7544	208.94	SHK86
4706	46069.7182	215.37	SHK86
9365	47566.3817	8.49	RvPT92
9368	47567.3466	109.96	RvPT92
10057	47788.6818	70.93	RvPT92
10060	47789.6457	85.99	RvPT92
10082	47796.7142	187.84	RvPT92
10088	47798.6401	53.81	RvPT92
22916	51919.5301	-12.64	This Paper
22922	51921.4577	0.21	This Paper

Similar values are found for V363 Aur with out-of-eclipse contributions of  $19 \pm 4$  per cent in blue and  $35 \pm 7$  per cent in red.

### 3.8 The $K_R$ Correction

The irradiation of the secondary stars in CVs by the emission regions around the white dwarf and the bright spot has been shown to influence the measured  $K_R$  (e.g. Wade & Horne 1988 and Watson & Dhillion 2001). For example, if absorption lines are quenched on the irradiated side of the secondary, the centre of light will be shifted towards the back of the star. The measured  $K_R$  will then be larger than the true (dynamical) value.

We must now determine whether the secondary stars in AC Cnc and V363 Aur are irradiated, which can be observationally tested in two ways. Firstly, the rotationally broadened line profile would be distorted if there was a non-uniform absorption distribution across the surface of the secondary star (Davey & Smith 1992). This would result in a non-sinusoidal radial velocity curve. Secondly, one would expect a depletion of absorption line flux from the secondary star at phase 0.5, where the quenched inner-hemisphere is pointed towards the observer (e.g. Friend et al. 1990). We applied these tests to the AC Cnc and V363 Aur data.

The secondary star radial velocity curves were produced by cross-correlating the CV spectra with the best-fitting smeared and broadened template spectra as described in Section 3.6. This time the cross-correlation peaks were plotted against phase to produce the radial velocity curves shown in the lower panels of Fig. 8. The radial velocity curves of both AC Cnc and V363 Aur are clearly eccentric in comparison to the sinusoidal fits represented by the thin solid lines.

The variation of secondary star absorption line flux with phase for AC Cnc and V363 Aur is shown in the top panels of Fig. 8. These lightcurves were produced by optimally subtracting the smeared and rotationally broadened best-fitting template from the individual CV spectra (with the secondary radial velocity shifted out) as described in Section 3.7. This time, however, the spectra were continuum subtracted rather than normalised to ensure that the measurements were not affected by a fluctuating disc brightness. The constants produced by the optimal subtraction are secondary star absorption line fluxes, correct relative to each other, but not in an absolute sense. The dashed lines superimposed on the lightcurves represent the variation of flux with phase for a Roche lobe with a uniform absorption distribution. The sinusoidal nature is the result of the changing projected area of the Roche lobe through the orbit. The lightcurves of AC Cnc and V363 Aur exhibit a drop in flux at phase 0.5 in comparison with the uniform Roche lobe.

These two pieces of evidence, as well as the observed Balmer emission from the inner hemisphere of the secondary stars seen in Figs. 3 and 4, and the weakening of the CCFs around phase 0.5 seen in Fig. 6 suggest that the secondary stars in AC Cnc and V363 Aur are indeed irradiated and we must correct the  $K_R$  values accordingly.

It is possible to correct  $K_R$  for the effects of irradiation by modelling the secondary star absorption line flux distribution. In our model, we divided the secondary Roche lobe into 40 vertical slices of equal width. We then pro-

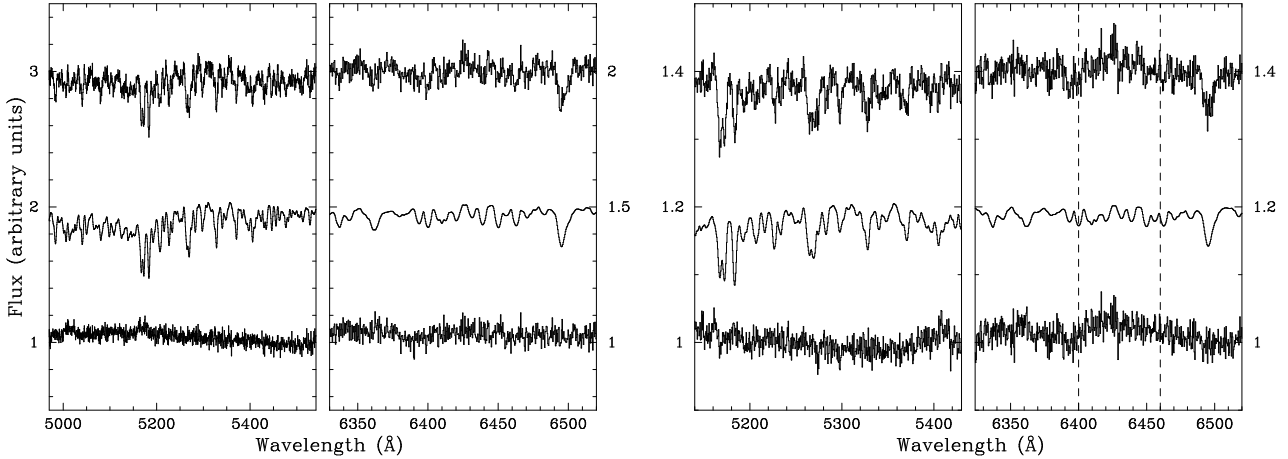


**Figure 7.** Orbitaly-corrected average eclipse spectra of the CVs (top) with the best-fitting broadened template (middle) and the residuals after optimal subtraction (bottom). The template spectra have been multiplied by the optimal factor found from the optimal subtraction. All of the spectra are normalised and have been offset on the plots by an arbitrary amount for clarity. Left: AC Cnc (eclipse phases  $-0.05 < \phi < 0.05$  in blue and red) with a K2V template. Right: V363 Aur (eclipse phases  $-0.07 < \phi < 0.09$  in blue and  $-0.09 < \phi < 0.09$  in red) with a G5V (red) and G7V (blue) template. The wavelength limits of the plots are those used for the cross-correlation and optimal extraction procedures for each object. The region between the dotted lines in the red spectrum of V363 Aur was omitted from the cross-correlation and optimal subtraction procedures due to the presence of a weak emission line. The average eclipse spectra shown (and the corresponding phase ranges listed above) are those used to determine the fractional contribution of the secondary stars given in Table 4.

duced a series of model lightcurves, varying the numbers of slices omitted from the inner hemisphere of the secondary which contribute to the total flux. The model lightcurves were then scaled to match the observed data, and the best-fitting model found by measuring the  $\chi^2$  between the two. In all models, we used a gravity-darkening parameter  $\beta = 0.08$  and limb-darkening coefficient  $u = 0.5$  (e.g. Watson & Dhillon 2001). There is evidence for a secondary eclipse in both systems, so we have omitted points around phase 0.5 from the fits. (We tried a model which included an accretion disc to reproduce the secondary eclipse, but the results were exactly the same as omitting the points.) Once the best-fitting lightcurve was found, we produced fake CV spectra from the models, which were cross-correlated with a fake template star to produce a synthetic radial velocity curve. In the first instance, the synthetic curve mimicked the non-sinusoidal nature of the observed data, but with a larger semi-amplitude. This was expected, as the model input parameters used the uncorrected  $K_R$  derived in Section 3.10. We then lowered  $K_R$  and repeated the process, until the semi-amplitude of the model and observed radial velocity curves were in agreement, each time checking the lightcurve models for goodness of fit. The resulting  $K_R$  was then adopted as the real (or dynamical)  $K_R$  value.

For AC Cnc, the best-fitting model lightcurve was produced by omitting 8 slices when fitting both the blue and red data. The model lightcurves omitting 7, 8 and 9 slices are shown by the solid lines in Fig. 8. Our final model, which has an input  $K_R$  of  $176 \text{ km s}^{-1}$ , produces the radial velocity curve shown as the thick solid line in Fig. 8. There is excellent agreement between this and the observed data. The best-fitting lightcurve models for V363 Aur have 10 slices omitted in blue and 8 slices in red. Model lightcurves omitting 9, 10 and 11 slices in blue and 7, 8 and 9 slices in red

are once again shown as solid lines in Fig. 8. The red data are very noisy, so we used the blue data to obtain a corrected  $K_R$  of  $168 \text{ km s}^{-1}$ . The model with this input value has the radial velocity curve plotted as the thick solid line in Fig. 8. It should be noted that if gravity-darkening and limb-darkening are neglected, the best fit lightcurves remain the same in all cases, and produce  $K_R$  values which are  $\sim 3 \text{ km s}^{-1}$  lower.

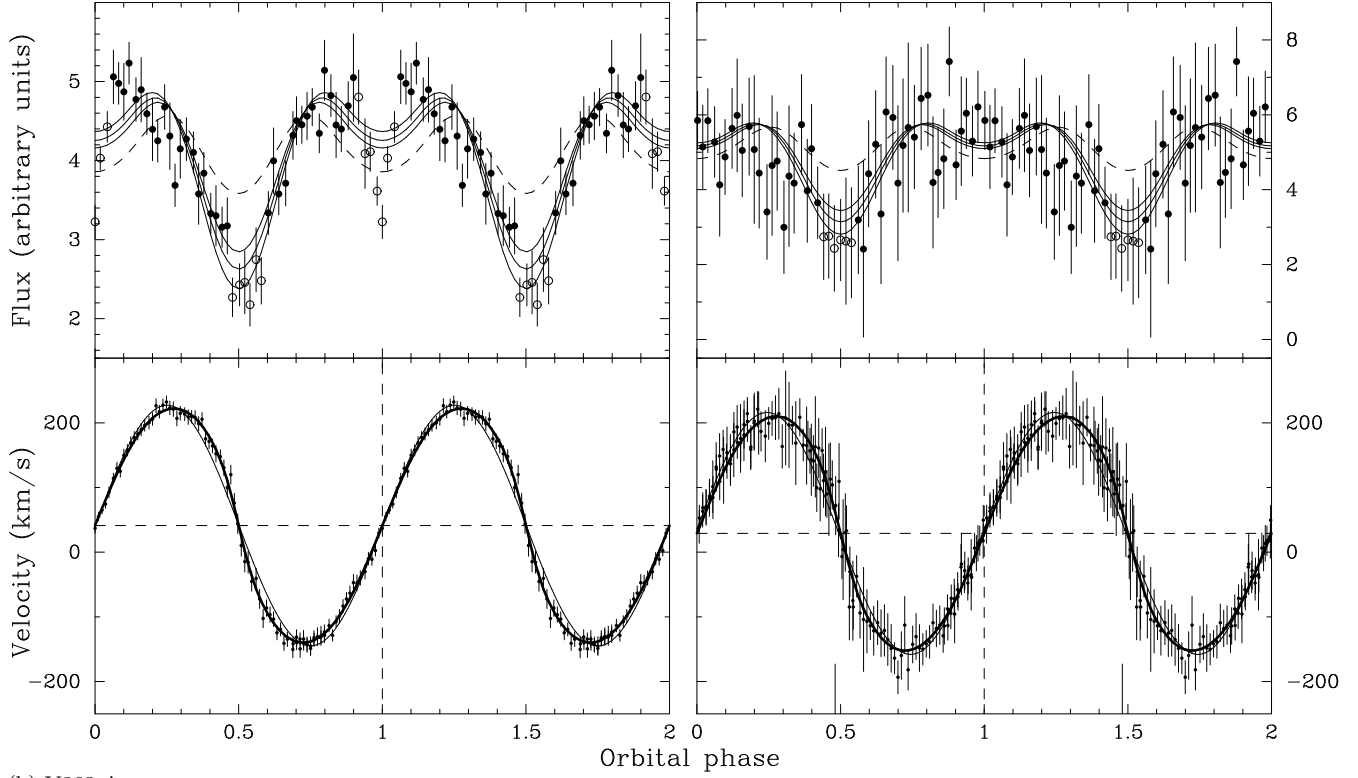
The points around primary eclipse in the blue lightcurve of AC Cnc were also omitted from the above fit, as they show a very sharp decrease in flux. Although some of this can be attributed to the reduced projected area of the secondary at phase 0, the feature is too sharp and too deep for this to be the only explanation. It is likely that this feature is an artefact of the slit-loss correction procedure, where  $B$ -band photometry has been used to correct secondary features which actually lie closer to the  $V$ -band. Because the  $B$ -band eclipse is deeper than the  $V$ -band eclipse, we get a residual sharp dip in the secondary star flux at phase 0. There is no corresponding dip in the red data, as the photometry and spectroscopy wavelengths are closely matched. There is no corresponding dip in flux at phase 0 in the blue V363 Aur data, even though both objects have been reduced in the same way. We believe this is because the  $V$ -band eclipse depth is approximately the same as the  $B$ -band eclipse depth in V363 Aur.

In summary, we correct the  $K_R$  of AC Cnc from  $186 \text{ km s}^{-1}$  to  $176 \text{ km s}^{-1}$  and the  $K_R$  of V363 Aur from  $184 \text{ km s}^{-1}$  to  $168 \text{ km s}^{-1}$ .

### 3.9 The distances to AC Cnc and V363 Aur

By finding the apparent magnitude of the secondary star from its contribution to the total light during eclipse, and

(a) AC Cnc



(b) V363 Aur

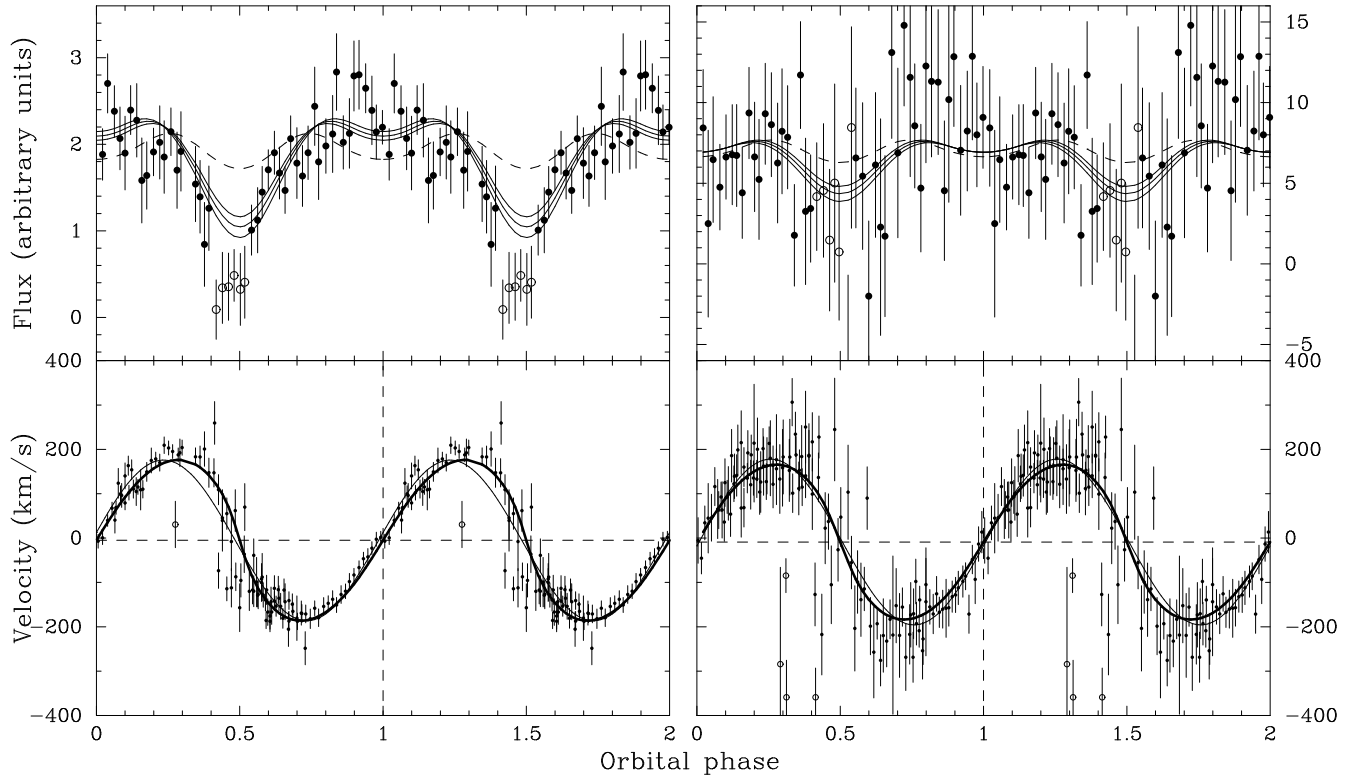


**Figure 8.** Upper panel: Secondary star lightcurves with model fits (solid lines). For AC Cnc, model fits are shown for Roche lobes with 7, 8 and 9 slices removed in both blue (left) and red (right). For V363 Aur, model fits are shown for Roche lobes with 9, 10 and 11 slices removed in blue (left) and 7, 8 and 9 in red (right). The lower the line, the more slices removed. The dashed line in all plots represents a model where 0 slices have been removed. The data have been phase-binned into 50 bins to increase signal-to-noise. Lower panel: Measured secondary star radial-velocity curve with a sinusoidal fit (thin solid line) and the best-fitting model fit (thick solid line). In all panels, the open circles indicate points that have been omitted from the fits and all data have been folded to show 2 orbital phases.

**Table 4.**  $v \sin i$  values (and minimum reduced  $\chi^2$ ) for AC Cnc and V363 Aur cross-correlated with the rotationally-broadened profiles of G5–K8 dwarf templates. Degrees of freedom: AC Cnc, 1143 (blue), 498 (red); V363 Aur, 580 (blue), 360 (red). Also shown is the fractional contribution of the secondary star to the total light during the eclipse phases, and the position of the strongest peak in the skewmaps when cross-correlated with each template using a  $\gamma$ -velocity of 40 km s<sup>−1</sup> for AC Cnc and 0 km s<sup>−1</sup> for V363 Aur.

(a) AC Cnc

Templates	min $\chi^2$ (blue)	$v \sin i$ at min $\chi^2$ (blue) km s <sup>−1</sup>	min $\chi^2$ (red)	$v \sin i$ at min $\chi^2$ (red) km s <sup>−1</sup>	Fractional contribution of secondary (blue)	Fractional contribution of secondary (red)	$(K_x, K_y)$ from skew map (blue) km s <sup>−1</sup>	$(K_x, K_y)$ from skew map (red) km s <sup>−1</sup>
G5V	1.081	142	1.106	136	1.24 ± 0.03	1.13 ± 0.10	(3,187)	(−4,185)
G6V	1.066	140	—	—	1.15 ± 0.03	—	(3,186)	—
G7V	1.038	140	—	—	1.18 ± 0.03	—	(−2,185)	—
G8V	1.046	141	1.100	137	1.20 ± 0.03	1.22 ± 0.11	(−1,186)	(−4,187)
G9V	1.080	139	1.097	136	1.19 ± 0.03	1.37 ± 0.12	(3,186)	(−4,186)
K0V	1.043	138	1.107	135	1.04 ± 0.02	0.99 ± 0.09	(1,185)	(−4,187)
K1V	—	—	1.112	134	—	0.93 ± 0.08	—	(−9,186)
K2V	1.038	136	1.112	134	0.85 ± 0.02	0.74 ± 0.07	(0,187)	(0,185)
K3V	1.127	134	—	—	0.82 ± 0.02	—	(−2,186)	—
K4V	1.406	138	1.137	131	0.62 ± 0.02	0.46 ± 0.04	(3,189)	(−2,185)
K5V	1.288	135	1.128	131	0.67 ± 0.02	0.56 ± 0.05	(0,187)	(−10,186)
K7V	1.319	136	1.125	130	0.65 ± 0.02	0.55 ± 0.05	(4,186)	(−3,186)
K8V	1.437	136	1.138	129	0.63 ± 0.02	0.50 ± 0.05	(0,188)	(−4,184)

(b) V363 Aur

G5V	1.081	148	1.119	139	0.25 ± 0.01	0.43 ± 0.07	(−7,184)	(10,185)
G6V	1.081	146	—	—	0.25 ± 0.01	—	(−8,184)	—
G7V	1.054	148	—	—	0.27 ± 0.01	—	(−13,181)	—
G8V	1.068	148	1.122	138	0.26 ± 0.01	0.46 ± 0.08	(−11,184)	(12,184)
G9V	1.098	143	1.120	140	0.24 ± 0.01	0.52 ± 0.09	(−4,183)	(13,185)
K0V	1.086	143	1.126	140	0.21 ± 0.01	0.37 ± 0.07	(−6,185)	(15,184)
K1V	—	—	1.120	138	—	0.37 ± 0.06	—	(7,189)
K2V	1.107	142	1.136	146	0.17 ± 0.01	0.29 ± 0.06	(−9,186)	(13,185)
K3V	1.150	139	—	—	0.17 ± 0.01	—	(−10,184)	—
K4V	1.294	134	1.140	146	0.10 ± 0.01	0.19 ± 0.04	(0,191)	(9,186)
K5V	1.234	134	1.132	141	0.11 ± 0.01	0.24 ± 0.04	(5,188)	(8,188)
K7V	1.252	132	1.134	145	0.11 ± 0.01	0.23 ± 0.04	(0,191)	(12,187)
K8V	1.297	134	1.138	148	0.10 ± 0.01	0.22 ± 0.04	(−4,188)	(8,187)

estimating its absolute magnitude, we can calculate the distance ( $d$ ) to each system using the equation:

$$5 \log(d/10) = m_V - M_V - d A_V/1000 \quad (5)$$

where  $A_V$  is the visual interstellar extinction in magnitudes per kpc.

There are a number of ways of estimating the absolute magnitude of the secondary star, assuming it is on the main sequence (e.g. Patterson 1984; Warner 1995b; Gray 1992). The distance estimates given below take into account all of these techniques.

Another method of finding the distance is to determine the angular diameter of the secondary star from the observed flux and a surface brightness calibration that we derive from the Barnes–Evans relation (Barnes & Evans 1976),

$$F_v = 4.2207 - 0.1V_0 - 0.5 \log \phi = 3.977 - 0.429(V - R)_0 \quad (6)$$

where  $V_0$  and  $(V - R)_0$  are the unreddened  $V$  magnitude and  $(V - R)$  colour of the secondary star, and  $\phi$  is the stellar angular diameter in arc milliseconds.

### 3.9.1 AC Cnc

During the eclipse phases given in Section 3.7, the average apparent magnitude of AC Cnc is  $R = 14.7 \pm 0.1$ , of which the secondary contributes  $74 \pm 19$  per cent, and  $B = 15.9 \pm 0.1$ , of which the secondary star contributes  $85 \pm 5$  per cent. The apparent magnitude of the secondary is therefore  $R = 15.0 \pm 0.3$  and  $B = 16.1 \pm 0.1$ . Using typical  $B - V$  and  $V - R$  values for an early K star from Gray (1992), we arrive at an apparent  $V$  magnitude of  $15.5 \pm 0.3$ . We adopt an absolute magnitude of  $M_V = +6.8 \pm 0.5$  as an average of the various methods referenced in the previous paragraph. Assuming zero interstellar extinction (la Dous 1991), the distance to AC Cnc is  $550 \pm 150$  pc.

Using the Barnes–Evans relation with a  $(V - R)_0$  value typical of an early K star ( $0.74 \pm 0.10$ ; Gray 1992), the  $V_0$  value of  $15.5 \pm 0.3$  found above and the radius of the secondary star derived in Section 3.10, we obtain a distance of  $750 \pm 250$  pc.

Published estimates of the distance to AC Cnc agree with our calculated values. Shugarov (1981) calculates a distance of 480 pc assuming a K5 secondary star. Patterson (1984) derives a value of 400 pc by com-

binning an  $M_V$ - $H\beta$  equivalent-width relationship, properties of the secondary and the continuum shape of the spectrum. Warner (1987) calculates a distance of 800 pc using the secondary star characteristics from Yamasaki, Okazaki & Kitamura (1983) and Zhang (1987) concludes  $d = 500 \pm 100$  pc, again estimating the secondary star properties.

### 3.9.2 V363 Aur

The average apparent magnitude of V363 Aur during the eclipse phases quoted in Section 3.7 is  $B = 14.8 \pm 0.1$  and  $R = 13.9 \pm 0.1$ , of which the  $G7 \pm 2V$  secondary star contributes  $25 \pm 3$  per cent and  $45 \pm 8$  per cent, respectively. This corresponds to an apparent magnitude of the secondary star of  $B = 16.3 \pm 0.2$ ,  $R = 14.8 \pm 0.2$  and, assuming typical  $B - V$  and  $V - R$  values for a  $G7 \pm 2V$  star (Gray 1992), we calculate  $V = 15.4 \pm 0.2$ . There is evidence of interstellar absorption in the average spectrum (Fig. 1), suggesting that it is important to take extinction into account. Szkody & Crosa (1981) give a value of  $E(B - V) = 0.3$ , although the UV spectrum used was underexposed and noisy. la Dous (1991), however, finds no extinction to V363 Aur, a result contradicted by measurements of Rutten, van Paradijs & Tinbergen (1992), who measure  $E(B - V) = 0.1$ . We adopt this value, which results in  $A_V = 0.32$  (Scheffler 1982). We use  $M_V = +6.0 \pm 0.5$  as an average absolute magnitude of the  $G7 \pm 2V$  star secondary star in V363 Aur, which results in a distance of  $700 \pm 250$  pc.

Using the Barnes-Evans relation with a  $(V - R)_0$  value typical of a mid-late G star ( $0.56 \pm 0.1$ ; Gray 1992), a  $V_0$  value of  $15.1 \pm 0.2$  assuming extinction to be 0.3 mag and the radius of the secondary star derived in Section 3.10, we obtain a distance of  $1000 \pm 250$  pc.

Szkody & Crosa (1981) estimate a distance to V363 Aur of 900 pc assuming a G0 dwarf secondary. Patterson (1984) derives an uncertain value of 1000 pc from the  $M_V$ - $H\beta$  equivalent-width relationship, interstellar absorption and the continuum shape of the spectrum. In his compilation of distances, Berriman (1987) gives a distance of 1100 pc from disc properties, 900–1300 pc from red star spectrophotometry and  $>450$  pc from the infrared properties of the secondary. Rutten, van Paradijs & Tinbergen (1992) calculate a distance of 530 pc from a black body fit to the spectrum of the central part of the disc and 720 pc using a value for the fractional contribution of the secondary.

### 3.10 System Parameters

Using the  $K_R$  and  $v \sin i$  values found in Sections 3.7 and 3.8 in conjunction with the period determined in Section 3.1 and a measurement of the eclipse full-width at half depth ( $\Delta\phi_{1/2}$ ), we can calculate accurate system parameters for AC Cnc and V363 Aur.

In order to determine  $\Delta\phi_{1/2}$ , we estimated the flux out of eclipse (the principal source of error) and at eclipse minimum, and then measured the full-width of the eclipse half-way between these points. The eclipse full-width at half-depth was measured to be  $\Delta\phi_{1/2} = 0.096 \pm 0.002$  for AC Cnc and  $0.063 \pm 0.002$  for V363 Aur from the  $B$  and  $R$ -band lightcurves in Fig. 2.

We have opted for a Monte Carlo approach similar to Horne, Welsh & Wade (1993) to calculate the system parameters and their errors. For a given set of  $K_R$ ,  $v \sin i$ ,  $\Delta\phi_{1/2}$  and  $P$ , the other system parameters are calculated as follows.

$R_2/a$  can be estimated because we know that the secondary star fills its Roche lobe (as there is an accretion disc present and hence mass transfer).  $R_2$  is the equatorial radius of the secondary star and  $a$  is the binary separation. We used Eggleton's formula (Eggleton 1983) which gives the volume-equivalent radius of the Roche lobe to better than 1 per cent, which is close to the equatorial radius of the secondary star as seen during eclipse,

$$\frac{R_2}{a} = \frac{0.49q^{2/3}}{0.6q^{2/3} + \ln(1 + q^{1/3})}. \quad (7)$$

The secondary star rotates synchronously with the orbital motion, so we can combine  $K_R$  and  $v \sin i$ , to get

$$\frac{R_2}{a}(1 + q) = \frac{v \sin i}{K_R}. \quad (8)$$

By considering the geometry of a point eclipse by a spherical body (e.g. Dhillon, Marsh & Jones 1991), the radius of the secondary can be shown to be

$$\left(\frac{R_2}{a}\right)^2 = \sin^2 \pi \Delta\phi_{1/2} + \cos^2 \pi \Delta\phi_{1/2} \cos^2 i, \quad (9)$$

which, using the value of  $R_2/a$  obtained using equations 7 and 8, allows us to calculate the inclination ( $i$ ) of the system. The geometry of a disc eclipse can be approximated to a point eclipse if the light distribution around the white dwarf is axi-symmetric (e.g. Dhillon 1990). This approximation is justified given the symmetry of the primary eclipses in the photometry light curves (Figure 2). Kepler's Third Law gives us

$$\frac{K_R^3 P_{orb}}{2\pi G} = \frac{M_1 \sin^3 i}{(1 + q)^2}, \quad (10)$$

which, with the values of  $q$  and  $i$  calculated using equations 7, 8 and 9, gives the mass of the primary star. The mass of the secondary star can then be obtained using

$$M_2 = qM_1. \quad (11)$$

The radius of the secondary star is obtained from the equation

$$\frac{v \sin i}{R_2} = \frac{2\pi \sin i}{P}, \quad (12)$$

(e.g. Warner 1995a) and the separation of the components,  $a$ , is calculated from equations 8 and 12 with  $q$  and  $i$  now known.

The Monte Carlo simulation takes 10 000 values of  $K_R$ ,  $v \sin i$ , and  $\Delta\phi_{1/2}$  (the error on the period is deemed to be negligible in comparison to the errors on  $K_R$ ,  $v \sin i$ , and  $\Delta\phi_{1/2}$ ), treating each as being normally distributed about their measured values with standard deviations equal to the errors on the measurements. We then calculate the masses of the components, the inclination of the system, the radius of the secondary star, and the separation of the components, as outlined above, omitting ( $K_R$ ,  $v \sin i$ ,  $\Delta\phi_{1/2}$ ) triplets which are inconsistent with  $\sin i \leq 1$ . Each accepted  $M_1, M_2$  pair is then plotted as a point in Figure 9, and the masses and their

errors are computed from the mean and standard deviation of the distribution of these pairs.

In the case of AC Cnc, we find that  $M_1 = 0.76 \pm 0.03 M_\odot$  and  $M_2 = 0.77 \pm 0.05 M_\odot$ ; for V363 Aur we find  $M_1 = 0.90 \pm 0.06 M_\odot$  and  $M_2 = 1.06 \pm 0.11 M_\odot$ . The values of all the system parameters deduced from the Monte Carlo computation are listed in Table 5, including  $K_R$ -corrected and non  $K_R$ -corrected values for comparison.

We computed the radius of the accretion discs in AC Cnc and V363 Aur using the geometric method outlined in Dhillon, Marsh & Jones (1991). The phase half-width of eclipse at maximum intensity was found in Section 3.3 to be  $\Delta\phi = 0.09 \pm 0.01$  for AC Cnc and  $\Delta\phi = 0.078 \pm 0.005$  for V363 Aur. Combining  $\Delta\phi$  with  $q$  and  $i$  derived above produces an accretion disc radius ( $R_D$ ) in terms of the volume radius of the primary's Roche lobe ( $R_1$ ). We find accretion disc radii of  $R_D/R_1 = 0.61 \pm 0.14$  and  $R_D/R_1 = 0.71 \pm 0.17$  for AC Cnc and V363 Aur, respectively, which are lower than those quoted by Harrop-Allin & Warner (1996), but consistent within the errors; AC Cnc:  $0.70 \leq R_D/R_1 \leq 0.86$ , V363 Aur:  $R_D/R_1 \geq 0.92$ .

The empirical relation obtained by Smith & Dhillon (1998) between mass and radius for the secondary stars in CVs is given by,

$$\frac{R}{R_\odot} = (0.93 \pm 0.09) \left( \frac{M}{M_\odot} \right) + (0.06 \pm 0.03). \quad (13)$$

This predicts that if the secondary stars in AC Cnc and V363 Aur are on the main-sequence, they should have radii of  $0.78 R_\odot$  and  $1.05 R_\odot$ , respectively. These values agree with our measured values of  $0.83 \pm 0.03 R_\odot$  and  $0.97 \pm 0.04 R_\odot$  to within the errors. Gray (1992) gives  $M = 0.76 M_\odot$  and  $R = 0.75 R_\odot$  for a K2 dwarf and  $M = 0.98 M_\odot$  and  $R = 0.96 R_\odot$  for a G5 dwarf, also in agreement with our measured values. We conclude that the secondaries in AC Cnc and V363 Aur are similar to main-sequence stars.

## 4 DISCUSSION

### 4.1 Are AC Cnc and V363 Aur SW Sex stars?

The SW Sex stars are a sub-class of NLs which have peculiar spectral properties – see Hellier 2000 and references therein for a summary of the current models. Most SW Sex stars share the following properties (e.g. Hoard et al. 2003):

- (i) They are usually high-inclination, eclipsing systems.
- (ii) Their spectra exhibit single-peaked emission lines rather than the double-peaked lines expected from near edge-on discs.
- (iii) The Balmer and HeI emission lines usually contain transient absorption cores, especially around photometric phase 0.5.
- (iv) They have high levels of excitation, with HeII  $\lambda 4686\text{\AA}$  emission often comparable in strength to H $\beta$ .
- (v) The low-excitation lines (Balmer and HeI) exhibit shallow or absent eclipses.
- (vi) High velocity S-waves are often seen in the trailed spectra.

(vii) The emission-line radial velocity curves show large phase shifts between spectroscopic conjunction and photometric mid-eclipse.

AC Cnc and V363 Aur show many of the features described above. V363 Aur shows all of the features, so must be considered a definite SW Sex star. AC Cnc does show high excitation features, but not to the extent of V363 Aur. Transient absorption features are seen in low-excitation lines of both systems. An interesting absorption feature also occurs around phase 0 in V363 Aur, which deserves further discussion.

The low-excitation emission lines of V363 Aur show the broad primary eclipse expected from a gradual obscuration of the accretion disc by the secondary (see Fig. 2). Around phase 0, however, there is a sharp increase in Balmer line emission followed by a rapid decrease. The feature comes and goes too rapidly to be attributable to a permanent emission source on the back of the secondary star. We suggest that this increase in flux can be explained by the eclipse of an optically thick region at the centre of the disc. The eclipse of this region, which would have an absorption line spectrum, would result in an overall increase in the line flux at the phases observed. Fig. 10 is the trailed spectrum of H $\beta$  magnified to show the effect more clearly. The blue wing of the line increases in flux first, in agreement with an eclipse of the centre of the disc. Fig. 11 is a reconstruction of V363 Aur using the  $K_R$ -corrected system parameters listed in Fig. 5. The left-hand diagram shows the system just before the increase in flux at phase 0.97, where the centre of the disc is just about to be eclipsed by the secondary. In the central diagram, the centre of the disc is eclipsed, corresponding to the brief rise in line flux. The right-hand diagram shows the system at phase 1.03, when the centre of the disc comes out of eclipse, and the line flux drops again. The short timescale of this feature is explained by the grazing nature of the eclipse of the optically thick region at the centre of the disc. This model could also account for the behaviour of other SW Sex stars where the Balmer lines show only a shallow eclipse compared to the continuum. Dhillon, Marsh & Jones (1997) and Groot, Rutten & van Paradijs (2001) suggest a similar explanation for SW Sex. The latter authors invoked an optically thick absorption-line source coincident with the bright spot, similar to that of a late B or early A-type star.

### 4.2 Mass Transfer Stability

The mass ratio ( $q = M_2/M_1$ ) of a CV is of great significance, as it governs the properties of mass transfer from the secondary to the white dwarf primary. This in turn governs the evolution and behaviour of the system.

The secondary star has two timescales on which it responds to mass loss. Firstly, the star returns to hydrostatic equilibrium on a dynamical timescale, which is the sound-crossing time of the region affected. Secondly, on a longer timescale, the star settles into a new thermal equilibrium configuration. The second timescale a star responds on is therefore the thermal, or Kelvin-Helmholtz, timescale.

The two timescales upon which the secondary responds to mass loss leads to two types of mass transfer instability. If, upon mass loss, the dynamical response of the secondary is to expand relative to the Roche lobe, mass transfer is

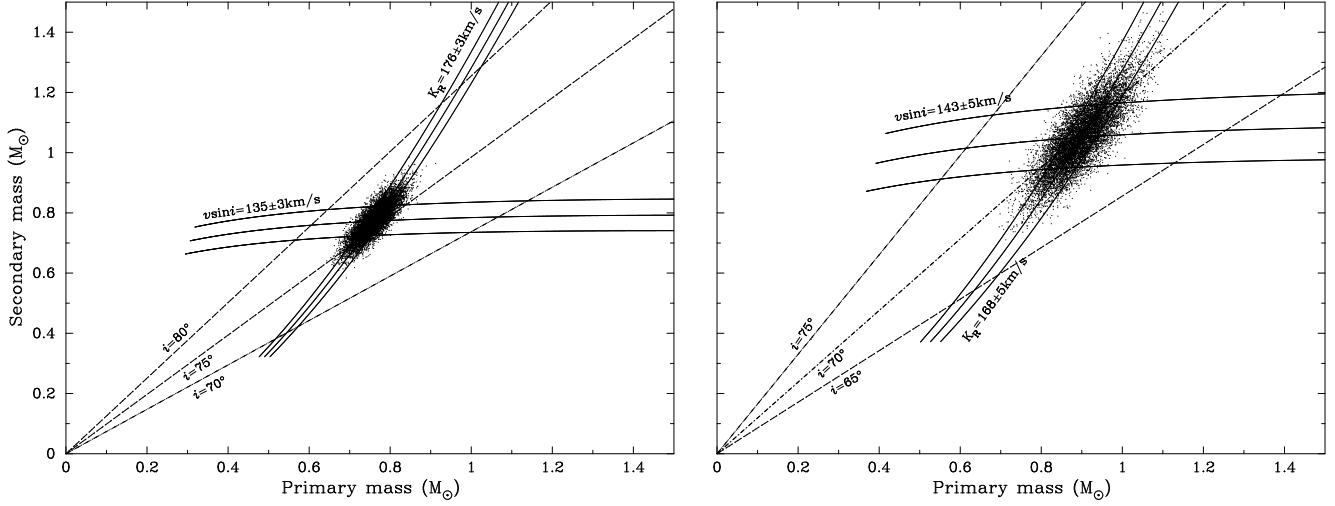


**Figure 9.** Monte Carlo determination of system parameters for AC Cnc (left) and V363 Aur (right). Each dot represents an  $M_1, M_2$  pair; the solid curves satisfy the  $v \sin i$  and corrected  $K_R$  constraints, and the dashed lines mark lines of constant inclination.

**Table 5.** System parameters for AC Cnc and V363 Aur. The Monte Carlo results for corrected and uncorrected  $K_R$  values are shown for comparison. The radial velocity of the white dwarf ( $K_W$ ) has also been calculated from the secondary star parameters. Distances are quoted using both techniques described in the text; by estimating the secondary star magnitude ( $d^{sec}$ ) and using the Barnes–Evans relation ( $d^{B-E}$ ).

Parameter	AC Cnc			V363 Aur		
	Measured Value	Monte Carlo Value	$K_R$ –corrected Value	Measured Value	Monte Carlo Value	$K_R$ –corrected Value
$P_{orb}$ (d)	0.30047747		0.30047747	0.32124187		0.32124187
$K_R$ (km s $^{-1}$ )	186 ± 3	186 ± 3	176 ± 3	184 ± 5	184 ± 5	168 ± 5
$v \sin i$ (km s $^{-1}$ )	135 ± 3	135 ± 3	135 ± 3	143 ± 5	143 ± 5	143 ± 5
$\Delta\phi_{1/2}$	0.096 ± 0.003	0.096 ± 0.003	0.096 ± 0.003	0.063 ± 0.002	0.063 ± 0.002	0.063 ± 0.002
$q$		0.94 ± 0.04	1.02 ± 0.04		1.04 ± 0.06	1.17 ± 0.07
$i^\circ$		76.3 ± 0.8	75.6 ± 0.7		70.5 ± 0.4	69.7 ± 0.4
$K_W$ (km s $^{-1}$ )		175 ± 6	179 ± 6		190 ± 9	196 ± 9
$M_1/M_\odot$		0.82 ± 0.04	0.76 ± 0.03		1.03 ± 0.07	0.90 ± 0.06
$M_2/M_\odot$		0.78 ± 0.05	0.77 ± 0.05		1.06 ± 0.11	1.06 ± 0.11
$R_2/R_\odot$		0.82 ± 0.02	0.83 ± 0.02		0.96 ± 0.04	0.97 ± 0.04
$a/R_\odot$		2.21 ± 0.04	2.18 ± 0.04		2.52 ± 0.07	2.47 ± 0.07
$d^{sec}$ (pc)	550 ± 150			700 ± 250		
$d^{B-E}$ (pc)	750 ± 250			1000 ± 250		
Spectral type of secondary	K2 ± 1 V			G7 ± 2 V		
$\Delta\phi$	0.09 ± 0.01			0.078 ± 0.005		
$R_D/R_1$			0.61 ± 0.14			0.71 ± 0.17

dynamically unstable and mass transfer proceeds on the dynamical timescale. Politano (1996) made an analytic fit to the models of Hjellming (1989) to give the limit of dynamically stable mass loss, plotted as the solid line in Fig. 12. Dynamically stable mass transfer can occur if the CV lies below this line. This limit is important for low mass secondary stars ( $M_2 < 0.5M_\odot$ ), as they have significant convective envelopes that tend to expand adiabatically in response to mass loss (de Kool 1992).

Thermally unstable mass transfer is possible if the dynamic response of the star to mass loss is to shrink relative to its Roche lobe (i.e. mass transfer is *dynamically* sta-

ble). This occurs at high donor masses ( $M_2 > 0.8M_\odot$ ) when the star has a negligible convective envelope and its adiabatic response to mass loss is to shrink (e.g. de Kool 1992; Politano 1996). Mass transfer then initially breaks contact and the star begins to settle into its new thermal equilibrium configuration. If the star’s thermal equilibrium radius is now bigger than the Roche lobe, mass transfer is again unstable, but proceeds on the slower, thermal timescale. The limit of thermally stable mass transfer can be found by differentiating the main–sequence mass–radius relationship given in Politano (1996). Thermally stable mass transfer can occur if the CV appears below the dotted line plotted in Fig. 12.



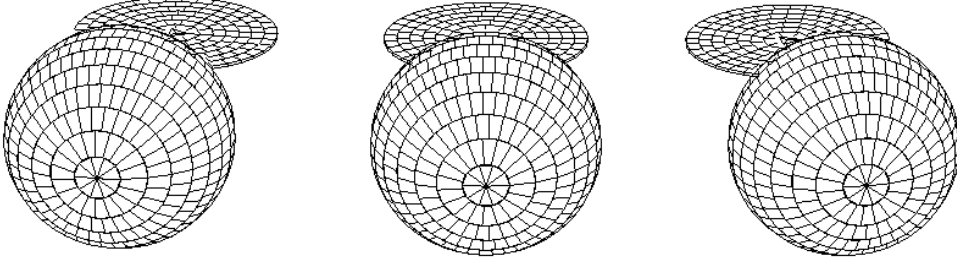


**Figure 11.** A model of V363 Aur using the  $K_R$ -corrected system parameters listed in Table 5. During primary eclipse, the secondary star grazes the absorption region at the centre of the disc, resulting in the rapid increase and then rapid decrease in Balmer flux seen in the trailed spectra at phase 0. The left-hand diagram shows the system at phase 0.97, the centre diagram at phase 1.00 and the right-hand diagram at phase 1.03.

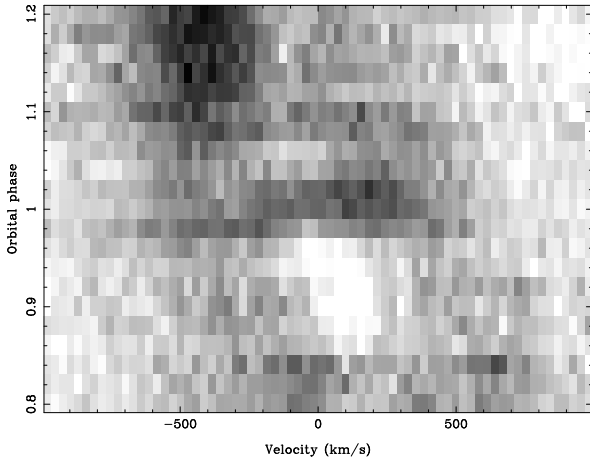


**Figure 10.** The V363 Aur H $\beta$  trailed spectrum, magnified to show the phases 0.8–1.2. The emission feature is clearly seen around phase 0, moving from blue to red.

Most CVs on the plot fall below both curves, implying that mass transfer is dynamically and thermally stable, as expected (the mass transfer rates observed in CVs are too low for unstable mass transfer to be occurring). An exception is DX And, which appears to be dynamically unstable. This is, of course, not possible; a system undergoing dynamical mass transfer would rapidly form a common envelope. A solution is found in the fact that DX And has an evolved secondary star (Drew, Jones & Woods 1993); the dynamical and thermal solutions plotted on Fig. 12 are for ZAMS stars, so cannot be applied to evolved stars.

The previous study of the masses of AC Cnc by Schlegel, Kaitchuck & Honeycutt (1984) found a  $q$  value of  $1.24 \pm 0.08$ , close to the limit for thermally stable mass transfer. In this study, we find a lower value of  $q = 1.02 \pm 0.04$ , placing it well within the theoretical limit. In the case of V363 Aur, we find a higher  $q$  value of  $1.17 \pm 0.07$  than the value of  $q = 0.90 \pm 0.10$  quoted by Schlegel, Honeycutt & Kaitchuck (1986), but it is still within the stability limit. The mass ratios found in this paper therefore place AC Cnc and V363 Aur within the region allowed by the theoretical constraints for stable mass transfer.

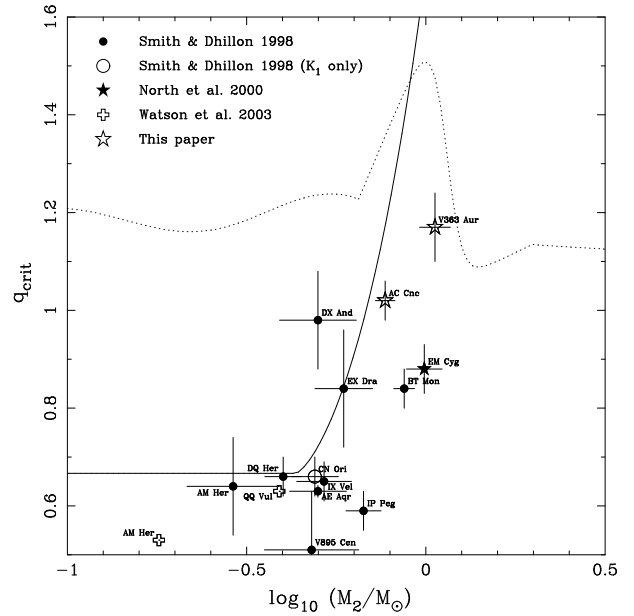


**Figure 12.** Critical mass ratios for mass transfer stability. The dotted line represents the condition for thermal instability; the solid line represents the condition for dynamical instability (Poltano 1996). Both curves assume the star is initially in thermal equilibrium. Mass ratios and secondary masses from the compilation of Smith & Dhillon (1998), North et al. (2000) and Watson et al. (2003) are overplotted. The mass ratios and secondary star masses of AC Cnc and V363 Aur determined in this paper are also plotted.

## ACKNOWLEDGEMENTS

We thank N. Samus and E. Zhang for providing eclipse timings of AC Cnc, and Homer Giannakis for help in reducing the photometry. We are indebted to Tom Marsh for the use of his software packages PAMELA and MOLLY, and we thank Uli Kolb, Stuart Littlefair and Tariq Shabaz for useful discussions. We also thank the referee, Robert Smith, for his careful reading of the manuscript and suggestions for improvements. TDT and MJS are supported by PPARC studentships; CAW is supported by PPARC grant number PPA/G/S/2000/00598. DS acknowledges a Smithsonian Astrophysical Observatory Clay Fellowship. The INT and JKT

are operated on the island of La Palma by the Isaac Newton Group in the Spanish Observatorio del Roque de los Muchachos of the Instituto de Astrofísica de Canarias.

## REFERENCES

- Barnes T. G., Evans D. S., 1976, *MNRAS*, 174, 489  
 Berriman G., 1987, *A&AS*, 68, 41  
 Davey S. C., Smith R. C., 1992, *MNRAS*, 257, 476  
 de Kool M., 1992, *AA*, 261, 188  
 Dhillon V. S., Jones D. H. P., Marsh T. R., 1994, *MNRAS*, 266, 859  
 Dhillon V. S., Marsh T. R., Jones D. H. P., 1991, *MNRAS*, 252, 342  
 Dhillon V. S., Marsh T. R., Jones D. H. P., 1997, *MNRAS*, 291, 694  
 Dhillon V. S., 1990, D. Phil thesis, University of Sussex  
 Downes R. A., 1982, *PASP*, 94, 950  
 Drew J. E., Jones D. H. P., Woods J. A., 1993, *MNRAS*, 260, 803  
 Eggleton P. P., 1983, *ApJ*, 268, 368  
 Friend M. T., Martin J. S., Smith R. C., Jones D. H. P., 1990, *MNRAS*, 246, 637  
 Gray D. F., 1992, *The Observation and Analysis of Stellar Photospheres*. Cambridge University Press, Cambridge  
 Groot P. J., Rutten R. G. M., van Paradijs J., 2001, *AA*, 368, 183  
 Harrop-Allin M. K., Warner B., 1996, *MNRAS*, 279, 219  
 Hellier C., 2000, *New Astronomy Reviews*, 44, 131  
 Helmer L., Morrison L. V., 1985, *Vistas in Astronomy*, 28, 515  
 Henden A. A., Honeycutt R. K., 1995, *PASP*, 107, 324  
 Hjellming M. S., 1989, PhD thesis, University of Illinois  
 Hoard D. W., Szkody P., Froning C. S., Long K. S., Knigge C., 2003, *AJ*, 126, 2473  
 Horne K., Lanning H. H., Gomer R. H., 1982, *ApJ*, 252, 681  
 Horne K., Welsh W. F., Wade R. A., 1993, *ApJ*, 410, 357  
 Knigge C., Long K. S., Hoard D. W., Szkody P., Dhillon V. S., 2000, *ApJ*, 539, L49  
 Kurochkin N. E., Shugarov S. Y., 1980, *Astron. Tsirk*, No. 1114  
 la Dous C., 1991, *AA*, 252, 100  
 Lanning H., 1973, *PASP*, 85, 70  
 Margon B., Downes R., 1981, *AJ*, 86, 747  
 Marsh T. R., Horne K., 1988, *MNRAS*, 235, 269  
 Marsh T. R., 1988, *MNRAS*, 231, 1117  
 Marsh T. R., 2001, in Boffin H., Steeghs D., Cuypers J., eds, *Proceedings of the International Workshop on Astro-tomography*, Brussels, July 2000. Springer-Verlag  
 Lecture Notes in Physics, Dusseldorf, p. 1  
 North R. C., Marsh T. R., Moran C. K. J., Kolb U., Smith R. C., Stehle R., 2000, *MNRAS*, 313, 383  
 Okazaki A., Kitamura M., Yamasaki A., 1982, *PASP*, 94, 162  
 Patterson J., 1984, *ApJS*, 54, 443  
 Politano M., 1996, *ApJ*, 465, 338  
 Rutten R. G. M., van Paradijs J., Tinbergen J., 1992, *AA*, 260, 213  
 Scheffler H. in Schaifers K., Voigt H. H., eds, *Landolt-Börnstein Numerical Data and Functional Relationships in Science and Technology*, New Series, Group VI, Vol. 2, Subvol. c, p. 47, Springer Verlag, Heidelberg, 1982  
 Schlegel E. M., Honeycutt R. K., Kaitchuck R. H., 1986, *ApJ*, 307, 760  
 Schlegel E. M., Kaitchuck R. H., Honeycutt R. K., 1984, *ApJ*, 280, 235  
 Schneider D. P., Young P. J., 1980, *ApJ*, 238, 946  
 Shafter A. W., Hessman F. V., Zhang E. H., 1988, *ApJ*, 327, 248  
 Shafter A. W., Szkody P., Thorstensen J. R., 1986, *ApJ*, 308, 765  
 Shugarov S. Y., 1981, *Sov. Astron.*, 25, 332  
 Smith D. A., Dhillon V. S., 1998, *MNRAS*, 301, 767  
 Smith D. A., Dhillon V. S., Marsh T. R., 1998, *MNRAS*, 296, 465  
 Spruit H. C., Rutten R. G. M., 1998, *MNRAS*, 299, 768  
 Szkody P., Crosa L., 1981, *ApJ*, 251, 620  
 Thoroughgood T. D., Dhillon V. S., Littlefair S. P., Marsh T. R., Smith D. A., 2001, *MNRAS*, 327, 1323  
 Vande Putte D., Smith R. C., Hawkins N. A., Martin J. S., 2003, *MNRAS*, 342, 151  
 Wade R. A., Horne K., 1988, *ApJ*, 324, 411  
 Warner B., 1987, *MNRAS*, 227, 23  
 Warner B., 1995a, *Cataclysmic Variable Stars*. Cambridge University Press, Cambridge  
 Warner B., 1995b, *Ap&SS*, 232, 89  
 Watson C. A., Dhillon V. S., 2001, *MNRAS*, 326, 67  
 Watson C. A., Dhillon V. S., Rutten R. G. M., Schwöpe A. D., 2003, *MNRAS*, 341, 129  
 Yamasaki A., Okazaki A., Kitamura M., 1983, *Publ. Astron. Soc. Japan*, 35, 423  
 Zhang E., 1987, *Acta Astrophysica Sinica*, 7, 245